10
Ab Initio Description of Thermoelectric Properties Based on the Boltzmann Theory

Nicki F. Hinsche, Martin Hölzer, Arthur Ernst, Ingrid Mertig, and Peter Zahn

10.1
Introduction

The conversion performance of a thermoelectric material is quantified by the figure of merit

$$ZT = \frac{\sigma S^2}{\kappa_{\mathrm{el}} + \kappa_{\mathrm{ph}}} T, \tag{10.1}$$

where σ is the electrical conductivity, S is the thermopower, and κ_{el} and κ_{ph} are the electronic and lattice contribution to the thermal conductivity, respectively. From Equation 10.1 it is obvious that a higher ZT is obtained by decreasing the denominator or by increasing the numerator, the latter being called power factor $\mathrm{PF} = \sigma S^2$. While σ, S, κ_{el} and κ_{ph} can individually be tuned by several orders of magnitude, the interdependence between these properties impedes high values of ZT [1, 2]. Bi_2Te_3, Sb_2Te_3, and their related alloys dominate the field of thermoelectrics with ZT around unity from the 1950s until now [3–5].

The idea of thermoelectric superlattices (SL) allows for concepts that could enable both the suppression of cross-plane thermal conductivity [6–8] and the increase of the electronic power factor [9–12]. It suggests that cross-plane transport along the direction perpendicular to the artificial interfaces of the SL reduces phonon heat conduction while maintaining or even enhancing electron transport [13].

In 2001 a breakthrough experiment by Venkatasubramanian *et al.* reported a record apparent $ZT = 2.4$ for p-type Bi_2Te_3/Sb_2Te_3 and $ZT = 1.4$ for n-type $Bi_2Te_3/Bi_2Te_{2.83}Se_{0.17}$ superlattices [8, 14, 15], although these values have not yet been reproduced to the best of our knowledge.

Thermoelectric Bi_2Te_3 Nanomaterials, First Edition.
Edited by Oliver Eibl, Kornelius Nielsch, Nicola Peranio, and Friedemann Völklein.

While considerable effort was undertaken in experimental research [16–23], theoretical investigations on Bi_2Te_3/Sb_2Te_3 SLs are rare. Available theoretical works concentrate on the electronic structure and transport properties of bulk materials [24–27], with some of them discussing the influence of strain, which could occur at the SL interfaces [28–30]. Based on density functional theory, Li *et al.* focused on the calculation of the electronic structure for two distinct Bi_2Te_3/Sb_2Te_3-SLs, stating changes of the mobility anisotropy estimated from effective masses [31, 32].

To clarify the open questions on the reduced mobility anisotropy and the enhanced thermoelectric efficiency, we discuss in this chapter the anisotropic thermoelectric electronic transport of seven different Bi_2Te_3/Sb_2Te_3-SLs, including the bulk materials, on the basis of density functional theory and semiclassical transport calculations.

For this purpose, the chapter is organized as follows. In the remaining part of Section 10.1 we discuss modern concepts to increase thermoelectric efficiency. In Section 10.2 we introduce our first principle electronic structure calculations based on density functional theory and the semiclassical transport calculations based on the solution of the linearized Boltzmann equation. In Section 10.3.1 we present results on the influence of strain on the TE properties of the bulk materials Bi_2Te_3 and Sb_2Te_3. The influence of different SL periods on electrical conductivity, thermopower, and the related power factor with a focus on their directional anisotropies is discussed in Section 10.3.2. To estimate the figure of merit, in Sections 10.3.3 and 10.3.4 results on the electronic contribution to the thermal conductivity and the Lorenz function and its deviation from the ideal value are presented. Section 10.3.5 is devoted to the calculation and analysis of phonon spectra of Bi_2Te_3.

10.1.1 Low-Dimensional Thermoelectrics

In 1993, the pioneering work of Hicks and Dresselhaus [33, 34] renewed the interest in thermoelectric (TE) research and became the inspiration for many of the recent developments in the field of low-dimensional thermoelectrics [35]. The basic idea is that quantum confinement of electrons and holes could dramatically increase the figure of merit ZT by increasing the power factor independently of the thermal conductivity. Quantum confinement is available in low-dimensional geometries as

zero-dimensional quantum dots (0D), one-dimensional nanowires (1D), as well as two-dimensional quantum wells and superlattices (SL, 2D).

While infinite enhancements of the in-plane figure of merit were predicted at vanishing layer thickness [33, 34, 36], electron tunneling and thermal currents were suppressed between the layers by introducing infinite potential barriers of zero width. Later on, it was shown that for realistic barrier heights and widths the enhancement is rather moderate, predicting ZT values a few percentage larger than the corresponding bulk materials [37–39]. Indeed, some groups found evidence for large enhancements of the thermopower in SLs based on PbTe [11, 40–43] and $SrTiO_3$ [44–47]. However, the determination of the 2D charge carrier concentration is sophisticated and led in at least two of the previous experiments [41, 43] to quite large estimates of the thermopower [48]. In some other model cases, the carriers had to be confined in delta-doped-like layers with a maximum width of a unit cell to show an enhancement up to $ZT \approx 2$ [44–46], while otherwise ZT would have been only marginally enhanced [49].

Several experiments have been performed on processing and characterizing TE 1D nanowires [50–56]. Confinement effects on the power factor $PF = \sigma S^2$ were negligible [39, 57]. While at very low wire diameters, $d \ll 15$ nm, enhancements of the power factor could be reached [39], the main gain in ZT for nanowires are caused by a strong reduction in the lattice thermal conductivity. Here, phonon scattering at the boundaries is the reason [51]. Unfortunately, at small diameters the latter effect causes a reduction in the phonon-drag effect and thus also in the thermopower [58]. If both phonon boundary scattering and phonon drag could be retained, promising values of ZT were found for TE nanowires [52].

Adding up the previous ideas, Mahan and Sofo [59] argued that sharp features in the electronic density of states (DOS) alone could lead to enhancements of the thermopower and the power factor. Recent experimental proofs of principle showed this assumption to be achievable already in bulk materials by the introduction of resonant defect levels close to the chemical potential [60–63].

10.1.2 Phonon-Glass Electron-Crystal

Obviously, the figure of merit ZT can be optimized either by enhancing the power factor σS^2 or by decreasing the thermal conductivity $\kappa_{el} + \kappa_{ph}$. For a long time, alloying achieved the lowest thermal conductivities [64].

The reduction of κ_{ph} is caused by the scattering of phonons by atomic substitutions and is limited by the so-called alloy limit. Unfortunately, the introduction of impurities leads also to electron-impurity scattering, which in most cases lowers the power factor.

At best, electron and phonon properties are decoupled, allowing for both maximizing the power factor and minimizing the lattice thermal conductivity at the same time. Having this in mind, Slack proposed the concept of phonon-glass electron-crystal in 1995 [65, 66]. The best TE material should possess thermal properties similar to that of a glass ($\kappa_{300\,K} \lesssim 1\,W/mK$ [67]) and electrical properties similar to that of a perfect single-crystal material [68]. To date, several experimental and theoretical studies supported this concept but differ in their approach.

Archetypical examples of bulk phonon-glass electron-crystal materials are the skutterudites ((Co,Ni,Fe)$(As,Sb)_3$ and related compounds) [68–71] and the clathrates (e.g. $Ba_8Ga_{16}Si_{30}$) [72–76].

A different approach to the phonon-glass electron-crystal concept was recently proposed by the Snyder group. Toberer *et al.* suggested that the lattice thermal conductivity scales inversely with the number of atoms in the unit cell [77–79]. This conjecture is supported in Figure 10.1(a), where the dependence of the lattice thermal conductivity on the unit cell volume is shown for different antimonides. With increasing unit cell volume, the number of atoms N increases, and with that the $3(N-1)$ optical phonon branches dominate for complex crystals. The bandwidth of the acoustic phonons thus reduces to $\Delta\omega_{acoustic} = N^{\frac{1}{3}}\omega_{max}$. The authors noted that the $3(N-1)$ optical modes have very small phonon group velocities and thus are assumed to account only for a constant, small, glass-like thermal conductivity within a Debye model [78, 80]. The latter assumption is rather crude. It is known that optical phonon modes can have group velocities in the same order as the acoustic modes and contribute significantly to κ_{ph} [81, 82]. However, the experimental results of Snyder *et al.* [77–79] for complex Zintl-phases showed a tremendous reduction of $\kappa_{ph} \approx 0.2\,W/mK$ along with $ZT \approx 1.3$ at high temperatures. Nevertheless, the intrinsically low κ_{ph} might be caused mainly by the complex crystal structures than by the proposed phonon velocity reduction.

The newest, maybe the most promising, member in the zoo of phonon-glass electron-crystal materials is bulk p-type $Cu_{2-x}Se$ [83]. Most interestingly, the Se atoms form a rigid face-centered cubic lattice providing a crystalline pathway for semiconducting holes, while the copper ions are highly disordered around the Se sublattice and show liquid-like mobility. This combination leads to a remarkable figure of merit $ZT = 1.5$

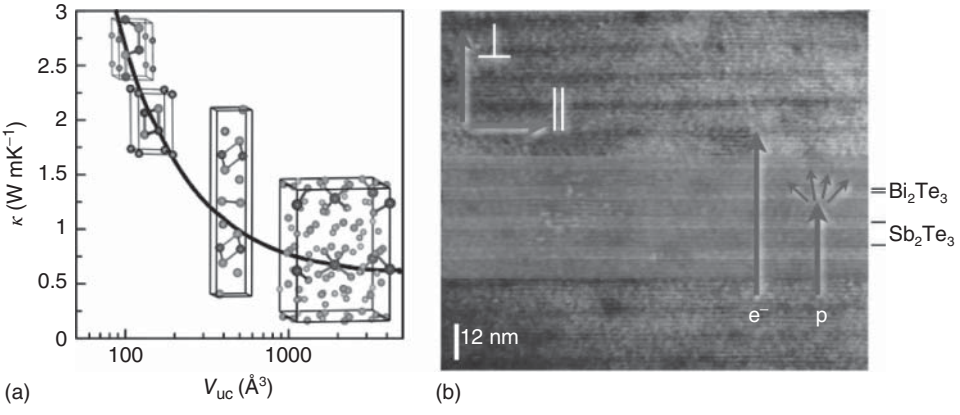

Figure 10.1 Complex thermoelectric materials within the phonon-glass electron-crystal approach. (a) Dependence of lattice thermal conductivity on the unit cell volume for different Zintl-antimonides. The lattice thermal conductivity rapidly decreases for increasing unit cell volume. Figure adapted with permission from Ref. [78]. Copyright (2010) American Chemical Society. (b) Transmission electron microscopy graphs (TEM) of a 10Å/50Å Bi_2Te_3/Sb_2Te_3-SL. Dark and light grey areas highlight the layered structure. For cross-plane transport (⊥) phonons (p) are expected to be scattered at the artificial interfaces, while electrons (e^-) transmit without losses. In the in-plane direction (||) quantum confinement effects for electrons are expected. Figure adapted with permission from Ref. [14]. Copyright (1999) American Institute of Physics.

together with $\kappa = 0.8$ W/mK at 1000 K. As a result, $Cu_{2-x}Se$ can be seen as an archetypical phonon-glass electron-crystal material.

10.1.3
Phonon-Blocking and Electron-Transmitting Superlattices

The very sophisticated TE concept of phonon-blocking and electron-transmitting (PBET) SLs combines the phonon-glass electron-crystal approach (Section 10.1.2 and the idea of quantum confinement in low-dimensional systems (Section 10.1.1). Made available by state-of-the art heteroepitaxy [13, 18, 84–87], SLs consist of alternating thin layers of different materials stacked periodically. The most prominent material combinations for TE SLs are Bi_2Te_3/Sb_2Te_3 [15, 18, 86, 88, 89], Si/Ge [90–92], and PbTe/PbSe [16, 41–43, 93, 94]. Other SLs based on Bi/Sb [95] or skutterudites [96] showed no or only small enhancements of the TE efficiency.

Despite being inspired by the approaches of a phonon-glass electron-crystal and the idea of quantum confinement in low-dimensional systems, the ansatz of a phonon-blocking electron-transmitting SL is very different.

First, they differ in their quantum confinement. In low-dimensional 1D, and 2D structures proposed by Hicks and Dresselhaus, the transport is mostly perpendicular to the confinement, c.f. along the in-plane direction of the SL, and can be assumed to be almost free-electron-like. In a phonon-blocking electron-transmitting SL the thermal gradient is preferably applied parallel to the confinement, c.f. electron and phonon transport occur in cross-plane direction of the superlattice. The latter is emphasized in Figure 10.1(b).

With no obvious enhancement of the cross-plane electronic transport to be expected due to quantum confinement effects, the desired increase in ZT has to stem entirely from a distinct reduction in the cross-plane lattice thermal conductivity $\kappa_{\mathrm{ph},\perp}$. Indeed, exceptionally low thermal conductivities were found for phonon-blocking electron-transmitting SLs [8, 42, 90, 97–99]. Venkatasubramanian *et al.* reported $\kappa_{\mathrm{ph},\perp} = 0.22\ \mathrm{W/mK}$ for Bi_2Te_3/Sb_2Te_3 SL with a period of 50Å, which is about five times smaller than the bulk values and significantly below the alloy limit [8]. Those values add up to the lowest room-temperature thermal conductivities in crystalline materials reported so far.

The physical reason for the low cross-plane thermal conductivity is still being intensely debated using two models [13]. In the first, the phonons are expected to be quasiparticles that are scattered specularly or diffusely at the interfaces [7]. Experimental results from Touzelbaev seem to support this model, as decreasing lattice thermal conductivity was found for an increased interface roughness [85]. In the second model, the phonons are expected to behave as coherent waves across the interfaces. Reduction in the thermal conductivity then comes purely from phonon dispersion effects, such as BZ downfolding, leading to decreased group velocities and thermal conductivities [100, 101]. This model alone is not sufficient to explain the magnitude of the thermal conductivity reduction perpendicular to the film plane, and it fails completely to explain the observed in-plane thermal conductivity reduction [13]. Venkatasubramanian proposed that coherent backscattering of phonons at mirror-like interfaces could lead to standing phonon waves that do not contribute to thermal transport. Depending on the SL period l, this leads to a localization of certain phonon modes with wavelength $\lambda \leq l/2$ [8]. The goal of SL engineering is to choose the SL period in such a way that low-frequency acoustic modes are localized and κ_{ph} is reduced.

At best, a phonon-blocking and electron-transmitting SL shows power factors similar to that of the bulk, albeit at different optimal carrier concentrations. As will be shown in the following, these assumptions are per

se rather optimistic but achievable under certain conditions. Summing up, TE transport in the cross-plane direction of SLs has achieved the highest values for the figure of merit so far. $ZT = 2.4$ and 1.5 were predicted for *p*-type and *n*-type Bi_2Te_3/Sb_2Te_3 SLs at room temperature [14], while $ZT = 1.6 - 3.5$ was reported for *n*-type PbSeTe-based quantum-dot superlattices at $T = 300 - 600\,\mathrm{K}$ [41–43]. Some of the measurements have been corrected after publication by the authors [48]. The maximum value of $ZT = 3.5$ is highly unlikely, but $ZT \gg 1$ is expected for all the samples.

10.2 Transport Theory

Based on the knowledge of the microscopic electronic structure of a material, the macroscopic TE transport properties can be obtained within the Boltzmann transport formalism [102, 103]. The generalized electronic transport coefficients are deduced in detail by solving a linearized Boltzmann equation in Section 10.2.1. With this, the thermoelectric transport processes are expressed and discussed by means of generalized forces and fluxes in Section 10.2.2. Solving the Boltzmann equation for the phonon distribution function provides insight into the lattice thermal conductivity (Section 10.3.5).

10.2.1 Linearized Boltzmann Equation and Relaxation Time Approximation

We restrict the following considerations to a time-independent external electric field $\mathscr{E}$ and a temperature gradient ∇T. Applying weak external fields, one can expect that a system in steady state will only slightly differ from its equilibrium distribution. Hence, it is appropriate that the occupation function f_k in the steady state can be separated into the equilibrium contribution f_k^0 given by the Fermi–Dirac distribution at temperature T and chemical potential μ and a modest perturbation g_k:

$$f_k = f_k^0 + g_k \qquad \text{with} \qquad f_k^0 = \frac{1}{e^{(E_k-\mu)/k_B T} + 1}. \tag{10.2}$$

The semiclassical equation of motion for the position $\mathbf{r}$ and the wave vector $\mathbf{k}$ can be used to describe the collision integral as the temporal change in the f_k due to the action of the external electric field $\mathscr{E}$ [102]. Assuming weak fields and small temperature gradients only, a linearized Boltzmann

equation is obtained. Assuming furthermore that the collision integral is proportional to the perturbation g_k divided by the relaxation time τ_k, the solution of the Boltzmann equation can be written as

$$g_k = \tau_k \mathbf{v}_\mathrm{k} \left[|e| \mathscr{E} + \frac{E_\mathbf{k} - \mu}{T} \nabla T \right] \frac{\partial f_k^0}{\partial E} \tag{10.3}$$

The derivativexs $\partial f_\mathrm{k}^0 / \partial E$ of the Fermi-Dirac distribution function indicates that only electrons within an energy shell in the order of $k_\mathrm{B} T$ near the Fermi surface can respond to the external forces. Those states have unoccupied states in their vicinity and are redistributed in **k**-space, as shown in Figure 10.2.

10.2.2
Transport Coefficients

While it has been discussed in the last section as to how a weak electric field and a thermal gradient alter the population of electronic states, one may conclude what electrical and heat currents **j** and **Q** occur in the steady state. Considering that $f_k = f_k^0 + g_k$ and that there is no spontaneous net current flow in equilibrium, only g_k of the perturbed occupation function f_k causes a current flow. Using Equation 10.3 the currents can be

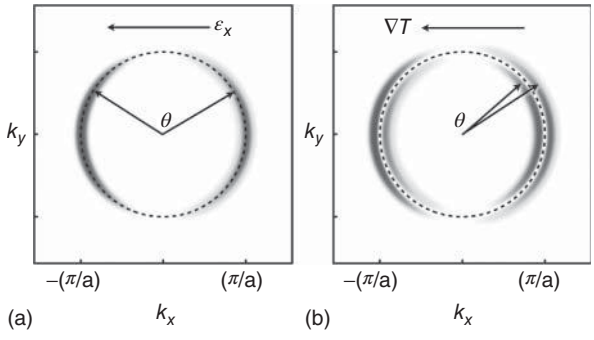

Figure 10.2 Schematic view of the distribution functions g_k on a slice cut through the k-space ($k_z = 0$) for a spherical Fermi surface. Two situations of electronic transport are considered. In (a), for an applied electric field along the negative x-direction; in (b) for a temperature gradient in the negative x-direction. The newly populated and depleted Brillouin zone areas are marked in grey. Note the distinction between the large-angle scattering (the so-called horizontal processes) in (a) and small-angle scattering connected with a change in the electron's energy (the vertical processes) in (b). The scattering angle between an initial and a final state is $\theta = (\mathbf{k}, \mathbf{k}')$ Original color figure can be found in *http://digital.bibliothek.uni-halle.de/urn/urn:nbn:de:gbv:3:4-10116*.

expressed by the generalized conductance moments $\mathscr{L}^{(n)}_{\perp,\parallel}(\mu, T)$, where n is the moment's order

$$\mathscr{L}^{(n)}_{(\parallel,\perp)}(\mu, T) = \int \mathrm{d}E\, \Sigma_{(\parallel,\perp)}(E) \cdot (E-\mu)^n \left(-\frac{\partial f^0_k(\mu, T)}{\partial E} \right)_{E_k=E}, \tag{10.4}$$

involving integrations over surfaces of constant electron energy E in reciprocal space:

$$\Sigma_{(\parallel,\perp)}(E) = \frac{1}{\hbar(2\pi)^3} \oint_{E_k=E} \frac{\mathrm{d}S}{|\mathbf{v}_\mathrm{k}|} \tau_k (\mathbf{v}_{\mathrm{k}(\parallel,\perp)})^2. \tag{10.5}$$

The directional indices '$\parallel$' and '$\perp$' denote the transport properties within and perpendicular to the basal plane of the layered systems considered here. For isotropic or cubic systems, this difference vanishes.

$\Sigma_{(\parallel,\perp)}(E)$ is the zeroth moment at vanishing temperature and coincides with the transport distribution function $\Sigma_{(\parallel,\perp)}(E) \equiv \mathscr{L}^{(0)}_{(\parallel,\perp)}(E, T=0)$ as introduced to thermoelectrics by Mahan and Sofo [59].

Using the above definitions, the electric and heat current densities can be written in terms of the generalized conductance moments

$$\mathbf{j} = e^2 \mathscr{L}^{(0)} \mathscr{E} - \frac{e}{T} \mathscr{L}^{(1)} \nabla T, \tag{10.6}$$

$$\mathbf{Q} = e \mathscr{L}^{(1)} \mathscr{E} - \frac{1}{T} \mathscr{L}^{(2)} \nabla T. \tag{10.7}$$

Depending on the boundary conditions certain transport coefficients can be derived, connecting acting fields and resulting quantities.

At a constant temperature, an electric current $\mathbf{j}$ flows in the material in response to an applied external electric field $\mathscr{E}$. Comparing Equation 10.6 with Ohm's law one reads

$$\mathbf{j} = \sigma \mathscr{E} \qquad \text{with} \qquad \sigma = e^2 \mathscr{L}^{(0)}, \tag{10.8}$$

where σ is the electric conductivity tensor. Here, $\sigma_{xx,zz} = \sigma_{\parallel,\perp}$ are the diagonal components within and perpendicular to the basal plane, respectively.

Assuming an electrical open circuit $\mathbf{j} = 0$ and applying a steady thermal gradient along the sample, the resulting electric field $\mathscr{E} = S \nabla T$ is given by

$$\mathscr{E} = \frac{1}{eT} \frac{\mathscr{L}^{(1)}}{\mathscr{L}^{(0)}} \boldsymbol{\nabla} T \qquad \text{with} \qquad S = \frac{1}{eT} \frac{\mathscr{L}^{(1)}}{\mathscr{L}^{(0)}}. \tag{10.9}$$

S is called the Seebeck coefficient or thermopower.

Combining the thermopower in Equation 10.9 with the electrical conductivity in Equation 10.8, for the thermoelectric power factor reads

$$\mathrm{PF} = \sigma S^2 = \frac{1}{T^2} \frac{(\mathscr{L}^{(1)})^2}{\mathscr{L}^{(0)}}, \tag{10.10}$$

which states the electrical power throughput of a material at a given temperature difference. The power factor strongly depends on the charge carrier concentration of the thermoelectric material and should be optimized to maximize the figure of merit ZT.

The electronic part of the total thermal conductivity accounts to

$$\kappa_{\mathrm{el},(\perp,\parallel)} = \frac{1}{T}(\mathscr{L}^{(2)}_{\perp,\parallel}(\mu, T) - \frac{(\mathscr{L}^{(1)}_{\perp,\parallel}(\mu, T))^2}{\mathscr{L}^{(0)}_{\perp,\parallel}(\mu, T)}), \tag{10.11}$$

with the heat current $Q_{\perp,\parallel} = -\kappa_{\mathrm{el}(\perp,\parallel)}\nabla T$.

The second term on the r.h.s. of Equation 10.11 introduces corrections due to the Peltier heat flow that can occur when bipolar conduction takes place [104, 105]. Using Equations 10.9 and 10.11 and the abbreviation $\kappa^0_{\mathrm{el}\perp,\parallel} = \frac{1}{T}\mathscr{L}^{(2)}_{\perp,\parallel}(\mu, T)$ [59], we find the Lorenz function as

$$L_{\perp,\parallel} = \kappa_{\mathrm{el},(\perp,\parallel)} \cdot (\sigma_{\perp,\parallel} \cdot T)^{-1}, \tag{10.12}$$

$$L_{\perp,\parallel} = \frac{\kappa^0_{\mathrm{el},(\perp,\parallel)}}{\sigma_{\perp,\parallel} T} - S^2_{\perp,\parallel}. \tag{10.13}$$

It clearly shows that in the low temperature regime the Lorenz function L consists of a constant term and a negative term of order T^2.

Boltzmann's transport theory can also be applied to phonons by simply taking into account the Boson occupation function

$$n^0_q = \frac{1}{e^{\frac{\hbar\omega_q}{k_B T}} - 1}, \tag{10.14}$$

where ω_q is the phonon energy dispersion, and q is a shorthand notation for the wave vector and the phonon branch number. Similar to the path described in section 10.2.1, one can derive the linearized phonon Boltzmann equation in relaxation time approximation (RTA) [102, 106–108]. Equivalent to Equation 10.5, the phonon heat conductivity $\kappa_{\mathrm{ph},(\parallel,\perp)}(T)$ can be expressed as

$$\kappa_{\mathrm{ph}}(T) = \int \mathrm{d}\omega\ \Sigma_{\mathrm{ph}}(\omega)\ C_V(\omega, T), \tag{10.15}$$

involving integrations over surfaces of constant phonon frequency ω,

$$\Sigma_{\mathrm{ph}}(\omega) = \frac{1}{8\pi^3} \oint_{\omega_q=\omega} \frac{\mathrm{d}S}{|\mathbf{v}_q|} \tau_q \mathbf{v}^2_q. \tag{10.16}$$

These properties are analogous to the electronic case in Equation 10.5 and include the phonon DOS $\mathscr{F}(\omega)$. Furthermore, the specific thermal heat at constant volume and temperature T is defined as

$$C_V(\omega, T) = \frac{(\hbar\omega)^2}{k_B T^2} n^0_\omega (n^0_\omega + 1). \tag{10.17}$$

10.3 Results

10.3.1 Influence of Strain

Before considering the Bi_2Te_3/Sb_2Te_3-SLs, the influence of strain on the thermoelectric properties of the bulk materials is discussed.

To this end, we used the experimental lattice parameters and relaxed atomic positions [109] as provided for the hexagonal Bi_2Te_3 crystal structure. The layered structure itself is represented by three quintuple units, $Te_1 - Bi - Te_2 - Bi - Te_1$. The hexagonal lattice parameters are chosen to be $a^{\text{hex}}_{\text{BiTe}} = 4.384\text{Å}$ and $c^{\text{hex}}_{\text{BiTe}} = 30.487\text{Å}$. The main difference between the lattices of Bi_2Te_3 and Sb_2Te_3 is mostly a decrease in the in-plane lattice constant with an accompanying decrease in cell volume. So, a change between the two lattice constants can be related to either compressive or tensile in-plane strain. Previous studies revealed that a larger in-plane lattice constant, c.f. $a^{\text{hex}}_{\text{BiTe}} > a^{\text{hex}}_{\text{SbTe}}$, is favorable for an enhanced cross-plane TE transport [26, 30, 110]. For this purpose, the experimental lattice parameters of Bi_2Te_3 were chosen for the heterostructures studied. To study SLs with different layer periods comparable to the experiments of Venkatasubramanian *et al.* we subsequently substituted the Bi sites by Sb, starting with six Bi sites in hexagonal bulk Bi_2Te_3 (see Figure 10.3(a)). For instance, substituting two atomic layers of Bi with Sb leads to a $(Bi_2Te_3)_x/(Sb_2Te_3)_{1-x}$ SL with $x = \frac{2}{3}$, that is, two quintuples Bi_2Te_3 and one quintuple Sb_2Te_3 (see Figure 10.3(b)). The latter case coincides with a (20Å/10Å)-(Bi_2Te_3/Sb_2Te_3) superlattice in the experimental notation of Ref. [15].

The dependence of anisotropy of the electrical conductivity on the in-plane conductivity $\sigma_{\parallel}$ for unstrained Bi_2Te_3 is shown in Figure 10.4(a). The temperature is fixed at 300K, the upper and lower parts of the loops refer to electron- and hole-doping, respectively. Based on a comparison with experimental data the in-plane relaxation time is determined to be $\tau_{\parallel} = 1.1 \times 10^{-14} s$ for Bi_2Te_3. The calculated dependencies of electrical conductivity on the thermopower and the electrical conductivity on the applied doping were matched to fit experiments [112–114]. With that, we find strong anisotropies for the electrical conductivity $\frac{\sigma_{\parallel}}{\sigma_{\perp}} \gg 1$, clearly preferring the in-plane transport. For the strongly suppressed cross-plane transport, p-type conduction is more favorable than n-type conduction. Pure band structure effects (solid lines in Figure 10.4(a)) result in overestimation of the measured anisotropy ratio [112] of the electrical conductivity.

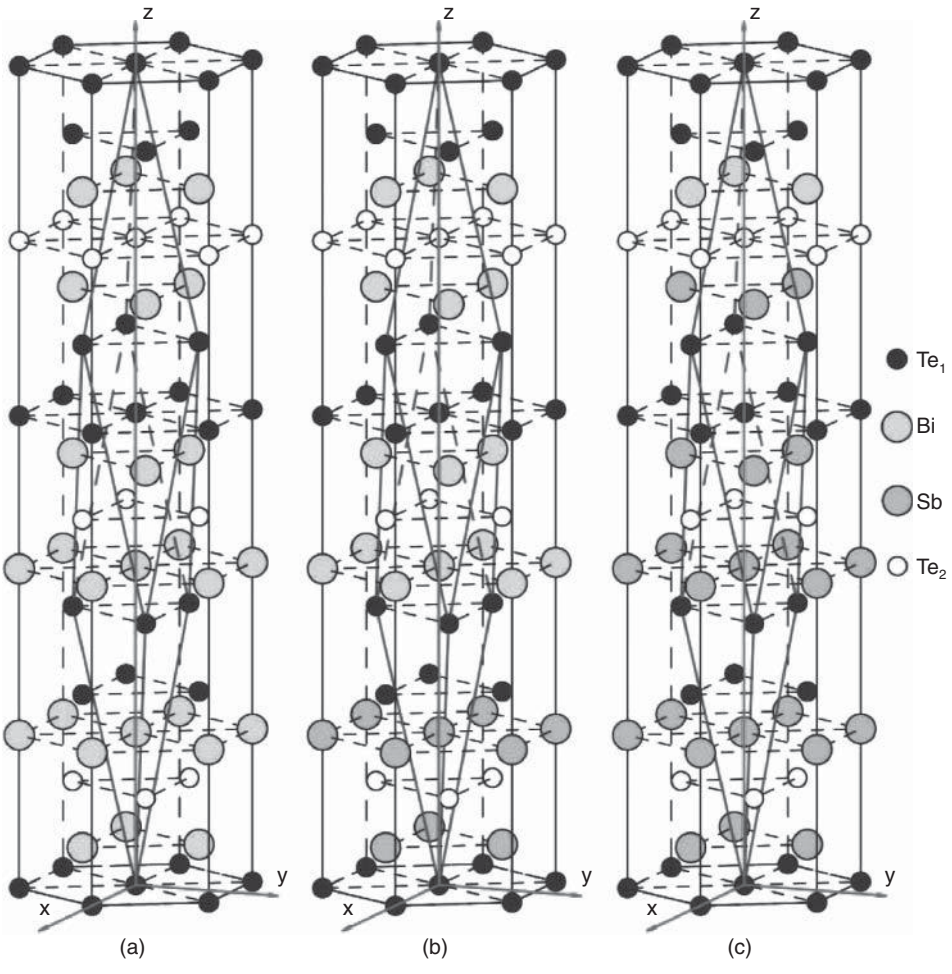

Figure 10.3 Shown are three possible hexagonal unit cells of the $(Bi_2Te_3)_x/(Sb_2Te_3)_{1-x}$ superlattices. (a) x=1, which is bulk Bi_2Te_3, (b) $x = \frac{2}{3}$, and (c) $x = \frac{1}{6}$. A concentration of x=0 would coincide with bulk Sb_2Te_3 in the lattice of Bi_2Te_3; with permission from Ref. [111], Copyright (2012) APS.

With an assumed anisotropy of the relaxation time of $\frac{\tau_{\parallel}}{\tau_{\perp}} = 0.47$ the experimental values are reproduced very well. This means that scattering effects strongly affect the transport, that is, electrons traveling along the basal plane direction are scattered more strongly than electrons traveling perpendicular to the basal plane. The origin of this assumed anisotropy has to be examined by defect calculations and the resulting microscopic transition probabilities and state-dependent mean free path vectors. It is well

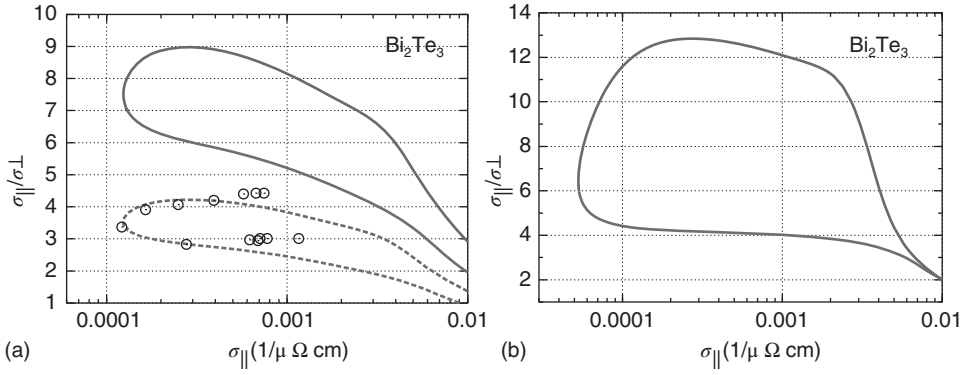

Figure 10.4 Ratio $\sigma_{\parallel}/\sigma_{\perp}$ of the electrical conductivities at 300K for (a) unstrained Bi_2Te_3 and (b) strained Bi_2Te_3 in the lattice structure of Sb_2Te_3. Electron doping refers to the upper parts of the loops, while the lower parts refer to hole doping. The dashed line in panel (a) present the ratio obtained with an anisotropic relaxation time $\frac{\tau_{\parallel}}{\tau_{\perp}} = 0.47$, while all other results are obtained with an isotropic relaxation time. Experimental data (circles) from Ref. [112] are given for comparison; with permission from Ref. [119], Copyright (2011) APS.

known that in Bi_2Te_3 mainly antisite defects lead to the inherent conduction behavior [115–117]. We have shown in Ref. [118] that integration of the transport integrals in Equation 10.5 in anisotropic k-space requires large numeric effort. Tiny regions in the k-space close to the band gap have to be scanned very carefully and the texture in the k-space has a drastic influence on the obtained anisotropy values, if integrals are not converged with respect to the *k*-point density. As shown, some integration methods tend for the given *k*-space symmetry to underestimate the ratio $\frac{\sigma_{\parallel}}{\sigma_{\perp}}$ in a systematic manner and therefore would shift anisotropy closer to the experimental observed values, without representing the real band structure effects.

For unstrained Bi_2Te_3, the electrical conductivity anisotropy is highest for low values of $\sigma_{\parallel}$, that is, small amounts of doping and bipolar conduction. For larger charge carrier concentrations, that is, the chemical potential shifts deeper into either conduction or valence band, the in-plane conductivity $\sigma_{\parallel}$ increases, and the ratio $\frac{\sigma_{\parallel}}{\sigma_{\perp}}$ decreases. Values for $\frac{\sigma_{\parallel}}{\sigma_{\perp}}$ will lower from 7 to 2 for *p*-type conduction and 9 to 3 for n-type conduction. However, cross-plane electrical transport is always more suppressed for *n*-type carrier conduction.

In order to understand the experimental findings on the in-plane and cross-plane transport, the anisotropies of the thermopower and

the related power factor of bulk Bi_2Te_3 are discussed in the following. Bulk Bi_2Te_3 is known to be inherently electron conducting, while hole doping is experimentally achievable for bulk systems [112, 113, 120, 121]. Figure 10.5 shows the variation of the anisotropic thermopower for unstrained Bi_2Te_3 in a wide temperature range. The extrinsic charge carrier concentration was fixed at $N = 1 \times 10^{19}\text{cm}^{-3}$. Experimental values for single crystalline material at the same doping conditions are given as a reference and excellent agreement is found. It is worth noting that within Equation 10.9 the calculation of the thermopower is completely free of parameters. The in-plane thermopower reaches a maximum of $S_{\parallel} \sim -200\mu\text{VK}^{-1}$ at 300 K, while the maximum for the hole-doped case is shifted to slightly higher temperatures of 350 K with a maximum value of $S_{\parallel} \sim 225\mu\text{VK}^{-1}$. We note that the temperature of the maximum is slightly overestimated. This might be caused by the missing temperature dependence of the energy gap, which was determined as $E_g = 105\,\text{meV}$ for unstrained Bi_2Te_3. Anisotropy of the thermopower is more pronounced for the p-doped case. Here, the cross-plane thermopower $S_{\perp}$ is always larger than the in-plane part $S_{\parallel}$ for the given doping concentration. The sole available experimental data do not show noticeable anisotropy for the thermopower in the hole-doped case [122]. For the electron-doped case the situation is more sophisticated. While up to 340 K the overall anisotropy is rather small, with values $\frac{S_{\parallel}}{S_{\perp}} \approx 0.9$, a considerable decrease in $S_{\perp}$ at higher temperatures leads to high values of $\frac{S_{\parallel}}{S_{\perp}}$ for temperatures above 400K. This tendency could also be revealed by experiments [115, 123]. The crossing point of $S_{\parallel}$ and $S_{\perp}$ near room temperature could explain the varying measured anisotropies for the thermopower at 300K. Here, anisotropy ratios of $\frac{S_{\parallel}}{S_{\perp}} = 0.97 \ldots 1.10$ were reported [115, 120]. The maximum peak of the thermopower near room temperature can be explained by the position of the chemical potential μ as a function of temperature at a fixed carrier concentration. For T values much smaller than 300K the chemical potential is located in either the conduction- or valence band with the tails of the Fermi–Dirac function in Equation 10.4 only playing a subsidiary role. For rising temperatures, the chemical potential shifts toward the band edges and S maximizes. Under these conditions, the conduction is mainly unipolar. For higher temperatures the chemical potential shifts into the band gap and conduction becomes bipolar, leading to reduced thermopower.

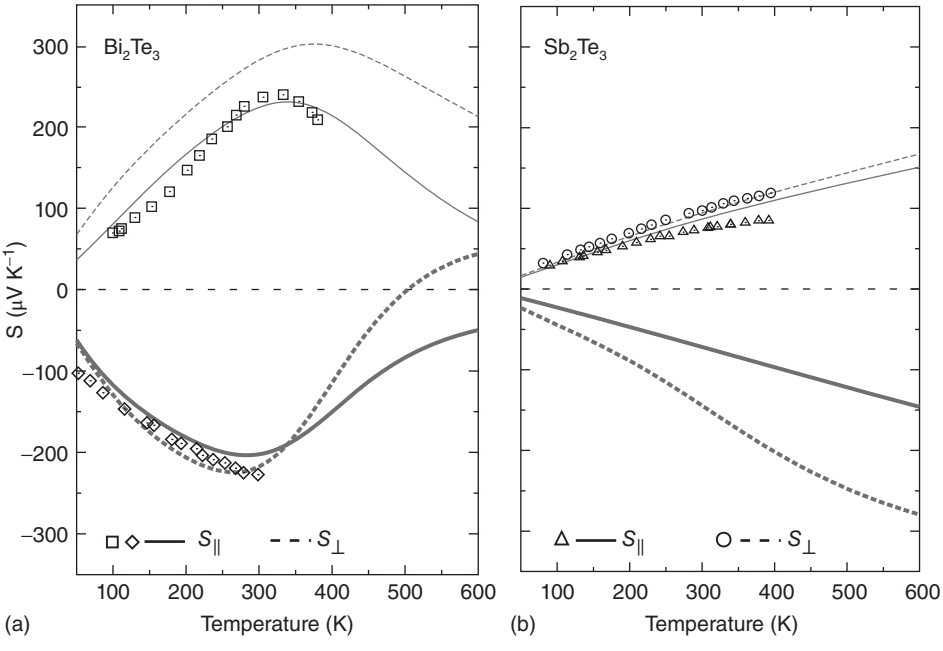

Figure 10.5 Anisotropic thermopower for bulk (a) Bi_2Te_3 and (b) Sb_2Te_3 in their unstrained bulk lattice structure. Electron doping refers to the thick lines in the lower part of the figure, while thin lines refer to hole doping and positive values of the thermopower. Solid lines show the in-plane part $S_{\parallel}$ of the thermopower, while dashed lines show the cross-plane part $S_{\perp}$. The extrinsic charge carrier concentrations of Bi_2Te_3 and Sb_2Te_3 were fixed at $N = 1 \times 10^{19}\text{cm}^{-3}$ and $N = 1 \times 10^{20}\text{cm}^{-3}$, respectively. Experimental data (squares, diamonds, circles, triangles) from Ref. [120, 122, 124] are given for comparison; with permission from Ref. [119], Copyright (2011) APS.

For the case of Sb_2Te_3, shown in Figure 10.5(b), the situation is different. Because of the ten times higher inherent doping and the smaller energy gap of $E_g = 90$ meV, the chemical potential is located deeply in the bands for the entire relevant temperature range. Therefore, the functional behavior can be understood in terms of the well-known Mott relation, where Equation 10.9 qualitatively coincides with $S \propto T \cdot \frac{\mathrm{d}\ln\ \sigma(E)}{\mathrm{d}E}|_{E=\mu}$ for the thermopower in relaxation time approximation [125]. With increasing temperature the thermopower increases almost linearly. The anisotropy of the thermopower for the hole-doped case is around $\frac{S_{\parallel}}{S_{\perp}} = 0.91$, almost temperature-independent and slightly underestimates the available experimental values [114, 126]. The anisotropy of the hole-doped case varies only weakly with temperature showing $\frac{S_{\parallel}}{S_{\perp}} = 0.48 \ldots 0.52$ over the

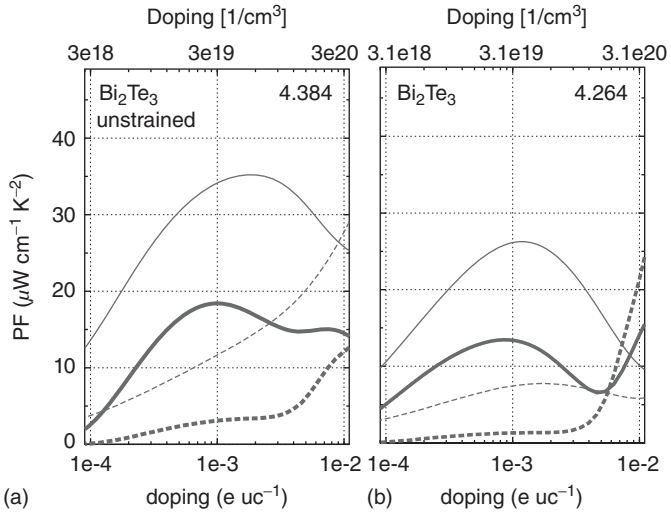

Figure 10.6 In-plane (solid lines) and cross-plane (dashed lines) doping-dependent Power factor at 300K for (a) Bi_2Te_3 in the Bi_2Te_3 structure and (b) Bi_2Te_3 in the Sb_2Te_3 structure. Electron (hole) doping is presented as thick (thin) line. The charge carrier concentration is stated in units of e/uc ($1cm^{-3}$) at the bottom (top) *x*-axis; with permission from Ref. [119], Copyright (2011) APS.

whole temperature range. While bulk Sb_2Te_3 shows a strong p-character due to inherent defects, we note here again that *n*-doping is available in heterostructures combining Bi_2Te_3 and Sb_2Te_3 [15].

In Figure 10.6(a) the doping-dependent anisotropic power factor of unstrained Bi_2Te_3 at room temperature is shown. Thick and thin solid lines represent the in-plane power factor $PF_{\parallel}$ under electron doping and hole doping, respectively. The corresponding cross-plane power factor $PF_{\perp}$ values are shown as dashed lines. Under p-doping, the unstrained material shows a maximum power factor near carrier concentrations of $N \sim 4 \times 10^{19} cm^{-3}$. An absolute value of $35\,\mu W/cmK^2$ was found for unstrained Bi_2Te_3, which is in good agreement with experimental and theoretical findings [17, 29, 127]. Under electron doping the absolute values of $PF_{\parallel}$ (thick lines in Figure 10.6) were found to be substantially smaller. This is due to smaller absolute values of the thermopower for electron doping compared to hole doping (see Figure 10.5) and apparently smaller in-plane electrical conductivities $\sigma_{\parallel}$ at fixed carrier concentrations. As a result, a power factor of $18\,\mu W/cmK^2$ is obtained under optimal electron doping.

Under applied in-plane compressive strain (cf. Figure 10.6(b)) decreases in the maximal power factor $PF_{\parallel}$ of about 27% and 23% for *n*-doping and *p*-doping were found, respectively. At a carrier concentration of about $N \approx 3 \times 10^{19}\text{cm}^{-3}$ the decrease in $PF_{\parallel}$ is about 17% and 28% for n- and p-doping, respectively, while in the work of Park *et al.* a slight increase of $PF_{\parallel}$ under strain and hole doping is reported [29]. Obviously, this trend can be understood by analyzing the constituent parts $\sigma_{\parallel}$ and $S_{\parallel}$, as discussed in Ref. [119].

10.3.2 Superlattices

While considerable effort was undertaken in experimental research [16–23], theoretical investigations on Bi_2Te_3/Sb_2Te_3 SLs are rare [31, 32]. Available theoretical works concentrate on the electronic structure and transport properties of the bulk materials [24–27], with some of them discussing the influence of strain, which could occur at the SL interfaces [28–30]. To clarify the open questions on the reduced mobility anisotropy and the enhanced thermoelectric efficiency, we are going to discuss in the following the anisotropic thermoelectric electronic transport of seven different Bi_2Te_3/Sb_2Te_3-SLs, including the bulk materials.

Here, we consider SLs $(Bi_2Te_3)_x/(Sb_2Te_3)_{1-x}$ SLs starting with $x = 0$, which is tensile strained bulk Sb_2Te_3, and ending at $x = 1$, which is bulk Bi_2Te_3. An increasing number of Bi layers in the SLs does not drastically change the band structure topology. Only slight variations were found for the in-plane band directions. A detailed discussion in given in Ref. [111]. In Figure 10.7 the dependence of the calculated band gap on the superlattice period is shown. Applying an extended tetrahedron method [128, 129] and very dense k-meshes in the Brillouin zone, the band gap values were determined within an uncertainty better than 1%. We obtain an indirect gap of $E_g = 140$ meV for the in-plane tensile strained Sb_2Te_3, which fits well with experimental values between $E_g = 150 - 230$ meV [130, 131]. For Bi_2Te_3 as well as for all Bi_2Te_3/Sb_2Te_3 SLs indirect band gaps are obtained, too.

The calculated bulk band gap of $E_g = 105$ meV for unstrained bulk Bi_2Te_3 is in agreement with the experimental value of $E_g = 130$ meV [130].

As is well known, Bi_2Te_3 and Sb_2Te_3 exhibit band inversion at certain areas in the Brillouin zone [132] where the strength of the spin orbit interaction controls the size of the band gap. Fortuitously, overestimated spin-orbit coupling effects and underestimated Density functional theory band gaps tend to cancel each other, leading to good results for the band gap size

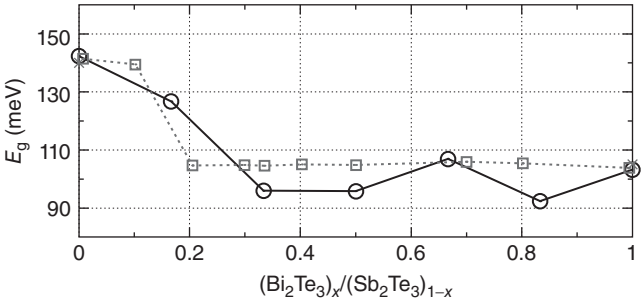

Figure 10.7 Dependence of the calculated fundamental band gap on the superlattice period (circles). Squares show experimental findings [130] for $(Bi_2Te_3)_x/(Sb_2Te_3)_{1-x}$ alloys, which were adapted to the bulk values to allow for comparison with our results (adapted with permission from Ref. [111]), Copyright (2012) APS.

and wave function character. The band gap difference between unstrained Bi_2Te_3 and strained Sb_2Te_3 accounts for about 35 meV, in very good agreement with the proposed value from experiment [15]. This is of particular importance for the discussion of quantum well effects below. An inclusion of temperature-dependent experimental band gaps will only have a minor influence, shifting the maxima of the thermopower, power factor, and resulting ZT (cf. Figure 10.9) to slightly larger values of the temperature.

While our calculated bulk band gaps are in very good agreement with other calculations [133–135], data on the SLs are rare [31]. To allow for a comparison of theoretical and experimental band gaps in Figure 10.7 the experimental values are scaled to agree with the theoretical ones for the bulk systems, that is, $x = 0$ and $x = 1$.

In the following, quantum well effects in the electronic structure are discussed. In the early 1990s concepts were presented to enhance in-plane thermoelectric properties by quantum-confinement effects in SLs [33, 34, 36]. While huge enhancements on the in-plane figure of merit were predicted, the authors neglected electron tunneling and thermal currents between the layers. Later on, it was shown that for realistic confinement parameters the enhancement is rather moderate [37, 136].

Our results show that a substitution of Sb and Bi in Bi_2Te_3 or Sb_2Te_3, respectively, affects the character of the valence band states only marginally, and almost bulk-like electronic structure and transport properties can be expected in the SLs. Bi_2Te_3 and Sb_2Te_3 show a theoretical band gap difference of about 35 meV; Thus, a band offset in the SL is expected. Our calculations reveal that this difference is mostly located in the conduction bands, which sets up potential barriers in the superlattice

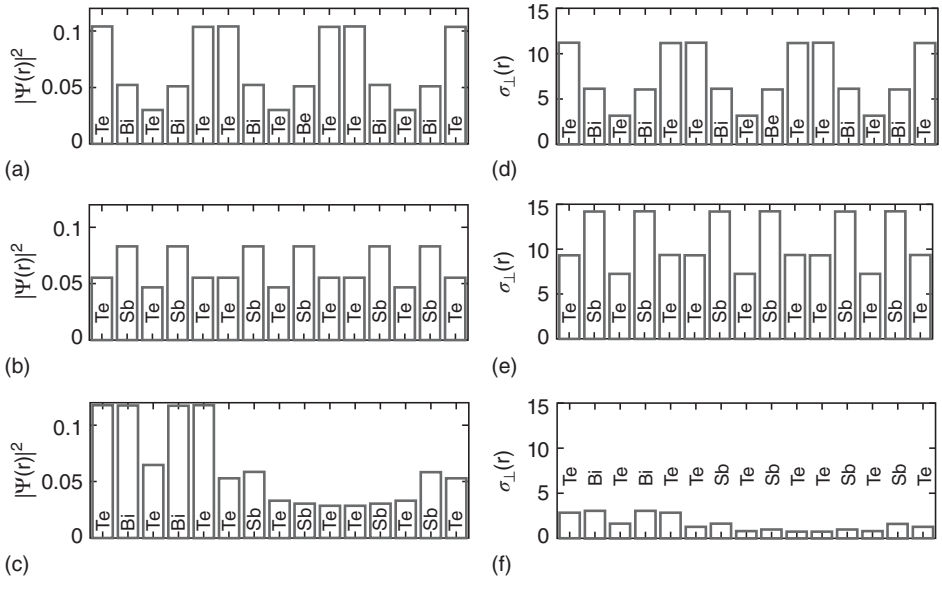

Figure 10.8 Site-resolved probability amplitude for (a) bulk Bi_2Te_3, (b) bulk Sb_2Te_3, and (c) a $(Bi_2Te_3)_x/(Sb_2Te_3)_{1-x}$ superlattice with $x = \frac{2}{6}$. In the same manner, the site-resolved cross-plane electrical conductivity $\sigma_\perp$ (in units of $(\Omega\text{cm})^{-1}$) is shown for (d) bulk Bi_2Te_3, (e) bulk Sb_2Te_3, and (f) a $(Bi_2Te_3)_x/(Sb_2Te_3)_{1-x}$ superlattice with $x = \frac{2}{6}$. The temperature is fixed at 300 K and the charge carrier concentration is set to $N = 3 \times 10^{19}\text{cm}^{-3}$, with permission from Ref. [111], Copyright (2012) APS.

leading to confinement effects. Therefore, the site-resolved probability amplitude for the two bulk tellurides, as well as for the superlattice, which showed the highest conductivity anisotropy, that is, 10Å/20Å Bi_2Te_3/Sb_2Te_3 SL ($x = \frac{2}{6}$), is shown in Figure 10.8(a)–(c). For Bi_2Te_3 the conduction band edge is dominated by contributions of the Te_1 followed by the Bi sites. A localization of states at the van der Waals gap is already visible in the bulk system. Areas of the BZ where no band inversion occurs dominate the CBM. For Sb_2Te_3 this is quite different. Most of the contributions to the conductivity arise from an area around the Γ point, where the band inversion favors the Sb character. As can be seen from Figure 10.8(b) the contributions to the DOS are equally distributed over all positions in the unit cell, while slightly being enlarged on the Sb sites. For the $(Bi_2Te_3)_x/(Sb_2Te_3)_{1-x}$ SL at $x = \frac{2}{6}$ (cf. Figure 10.8(c)) we found quantum well states, which localize about half of the density in the Bi_2Te_3 quintuple, while the density in the two Sb_2Te_3 quintuples is strongly depleted.

As shown in Figure 10.8(f), the quantum confinement is reflected in the contribution to the cross-plane electrical conductivity. Here, the local contribution to the cross-plane conductivity $\sigma_\perp(\mathbf{r})$ is calculated as introduced in Ref. [137], by weighting the contributions to $\mathscr{L}^{(0)}_{\perp,\parallel}(\mu, T)$ with the normalized probability amplitude $|\Psi(\mathbf{r})|^2$ of the electronic states at chemical potential μ. Summing up $\sigma_\perp(\mathbf{r})$ over all sites in the unit cell gives the total electrical conductivity $\sigma_\perp$ (cf. Figures 3(a) and 4(a) in Ref. [111]).

Nevertheless, sites in the Bi_2Te_3 quintuple with more accumulated density carry a larger contribution to the conductivity $\sigma_\perp$; the total contribution compared to the bulk tellurides is strongly suppressed (cf. Figure 10.8(d),(e)). This can be affirmed by a picture that electrons traveling in the cross-plane direction are governed by suppression of the probability amplitude in the Sb_2Te_3 quintuples. This clearly leads to a diminished cross-plane group velocity of the electronic states. Furthermore, comparing Figures 10.8(d) and (e), even the localization inside the quintuple in bulk Bi_2Te_3 can lead to reduced cross-plane electronic transport, reflected in larger total anisotropies of about $\frac{\sigma_\parallel}{\sigma_\perp} = 8$ for bulk Bi_2Te_3 compared to $\frac{\sigma_\parallel}{\sigma_\perp} = 5$ for bulk Sb_2Te_3.

10.3.3
Thermal Conductivity - Toward the Figure of Merit

With the electronic transport properties discussed in the previous sections, we now focus on the electronic and lattice part contribution to the thermal conductivity $\kappa_{el} + \kappa_{ph}$ to give some estimations for ZT. As has been stated already, the main benefit from a superlattice structure for ZT is expected from a reduction of the cross-plane thermal conductivity at retained electronic transport properties. Today, the reduction of the cross-plane lattice thermal conductivity in thermoelectric superlattices has been widely and successfully proved [90, 91, 97, 98]. In the past, thermal conductivity reduction in crystalline or polycrystalline bulk thermoelectric materials was traditionally achieved by alloying. However, one reaches the so-called “alloy limit” of thermal conductivity, which has been difficult to surpass by nanostructuring [2]. Nevertheless, for Bi_2Te_3/Sb_2Te_3 SLs cross-plane lattice thermal conductivites of $\kappa_{ph} = 0.22\ \mathrm{W/mK}$ were reported for certain SL periods, which is a factor of two below the alloy limit [8]. It is obvious, that at thermoelectrically relevant charge carrier concentrations and temperature ranges, the electronic contribution κ_{el} can be in the same order of magnitude.

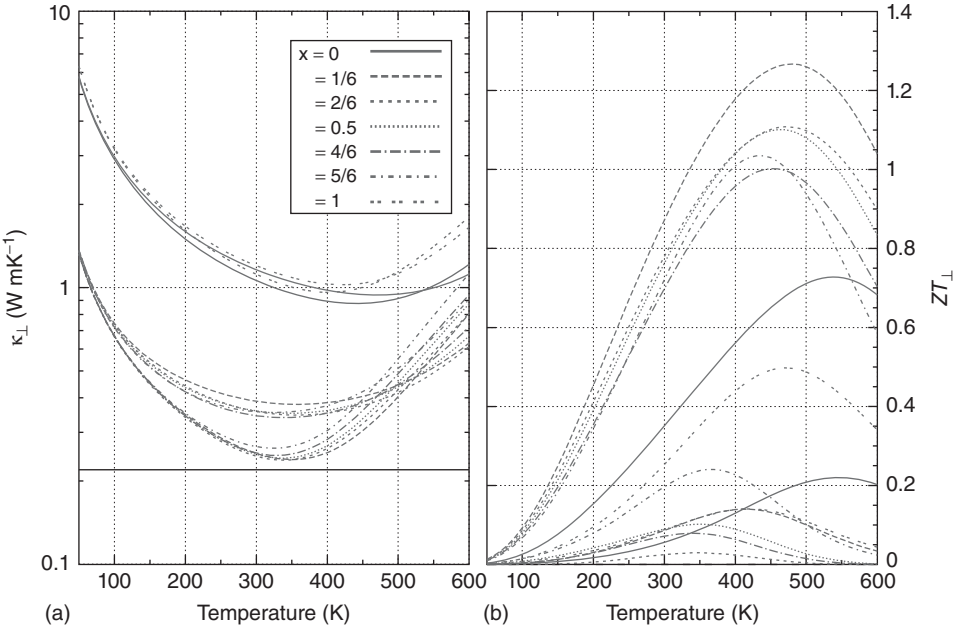

Figure 10.9 Temperature dependence of the thermal conductivity and figure of merit for the $(Bi_2Te_3)_x/(Sb_2Te_3)_{1-x}$ SLs. Shown are (a) total cross-plane thermal conductivity $\kappa_\perp = \kappa_{el,\perp} + \kappa_{ph,\perp}$ and (b) cross-plane figure of merit. The charge carrier concentration is fixed at $N = 3 \times 10^{19}$cm^{-3}, and different line types correspond to different SL periods. Lines in the upper part refer to electron doping, while lines in the lower part refer to hole doping. The electronic part κ_{el} was calculated, while the lattice part κ_{ph} was taken from literature [8, 15]; with permission from Ref. [111] (color online), Copyright (2012) APS.

Experimental findings for the lattice part κ_{ph} of the thermal conductivity are added to the calculated electronic contribution κ_{el} to present some estimations on the cross-plane $ZT_\perp$ in Figure 10.9. In particular $\kappa_{ph,\perp} = 1.05$ W/mK, $\kappa_{ph,\perp} = 0.96$ W/mK, and $\kappa_{ph,\perp} = 0.22$ W/mK at room temperature were used for bulk Bi_2Te_3, Sb_2Te_3, and the Bi_2Te_3/Sb_2Te_3 SLs [8], respectively. Recently, Winkler *et al.*[23] measured for a p-type $(Bi_{0.2}Sb_{0.8})_2Te_3/Sb_2Te_3$ SL the total cross-plane thermal conductivity $\kappa_\perp$ to be about $0.45 - 0.65$ W/mK for different annealing temperatures, which are smaller values than found in Ref. [15]. This is caused by a strong electrical conductivity anisotropy $\frac{\sigma_\parallel}{\sigma_\perp}$. Hence, the charge and electron heat transport in the perpendicular direction is noticeably suppressed. Additional obstacles for phonon heat transport are the nanocrystallinity of the samples and interface roughness, which is most likely caused by interdiffusion processes during the growth of Bi_2Te_3/Sb_2Te_3 SLs within

the concept of "nanoalloying" [18, 23]. Temperature-dependent results for the cross-plane figure of merit ZT are shown for the $(Bi_2Te_3)_x/(Sb_2Te_3)_{1-x}$ SLs at electron/hole concentration of $N = 3 \times 10^{19}\text{cm}^{-3}$ in Figure 10.9. Owing to the lack of detailed experimental data, we assumed a conventional $\frac{1}{T}$ dependence for the lattice thermal conductivity [138], while we note that temperature-independent κ_{ph} were confirmed experimentally for other thermoelectric SLs [90, 91, 139]. Models show that κ_{ph} should diminish at low periods[140], while experiments reveal a saturation toward the alloy limit for SL periods below 50Å [8].

Combining the results for $\kappa_{\text{ph},\perp}$ with the temperature-dependent power factor $\text{PF}_\perp$ discussed in Figure 6(d) of Ref. [111] we find the temperature dependence of the cross-plane $ZT_\perp$ values of the superlattices as presented in Figure 10.9b). Focusing on the more promising p-type SLs we found enhanced values for $ZT_\perp$ clearly above unity for temperatures of 400 – 500 K. The largest cross-plane figure of merit is found to be $\text{ZT}_\perp = 1.27$ at about 470 K for a $(Bi_2Te_3)_x/(Sb_2Te_3)_{1-x}$ SL at $x = \frac{1}{6}$ and a hole concentration of $N = 3 \times 10^{19}\text{cm}^{-3}$. We want to mention that in the experiments of Ref. [15] the maximal $ZT_\perp$ under hole doping was stated at a SL period of $x = \frac{1}{6}$, too. The best value for an n-type SL is $ZT_\perp = 0.25$ at about 360 K for a SL period of $x = \frac{5}{6}$.

In summary, the figure of merit can be slightly increased in SL structures if the electronic transport is maintained at the level of the bulk materials such as here for the hole-doped case, and the thermal transport is reduced by the layered structure.

10.3.4 Lorenz Function of Superlattices

We want to start our discussion of the Lorenz function with a model consideration. The Lorenz function L and the corresponding electronic thermal conductivity κ_{el} in dependence on the chemical potential μ are shown for a spherical two band model (SBM) in Figure 10.10. Results for varying effective mass ratios $\frac{m_{CB}}{m_{VB}}$ at a fixed temperature $T = 450$ K are shown. m_{CB} and m_{VB} are the isotropic effective masses of the conduction band (CB) and valence band (VB), respectively. Setting the valence band maximum to zero and E_g the band gap size, the transport distribution function scales as $\mathscr{L}^{(0)}_{\text{VB}}(\mu, 0) \sim \sqrt{m_{\text{VB}}}(-\mu)^{3/2}$ and $\mathscr{L}^{(0)}_{\text{CB}}(\mu, 0) \sim \sqrt{m_{\text{CB}}}(\mu - E_{\text{g}})^{3/2}$ for the VB and CB, respectively. From Equations 10.11 and 10.13 it is obvious that within a SBM deviations for L and κ_{el} from the metallic limit will merely occur near the band gap, where the thermopower S changes significantly.

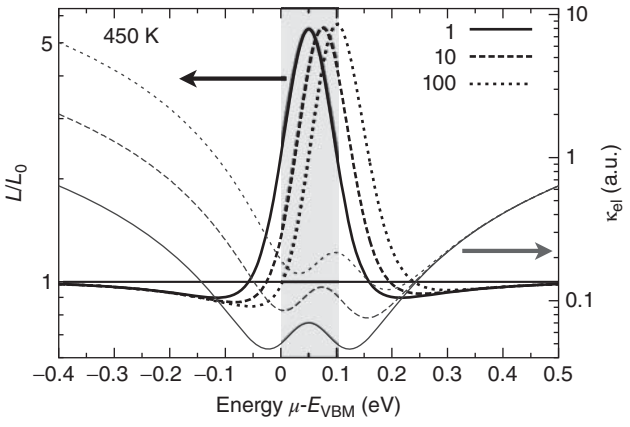

Figure 10.10 Lorenz function L (thick lines, ref. to left scale) and electronic contribution κ_{el} to the total thermal conductivity (thin lines, ref. to the right scale) in dependence on position of the chemical potential μ within a spherical two band model. Results are shown for a fixed temperature $T = 450$ K and varying effective mass ratios $m_{VB}/m_{CB} = 1 \ldots 100$. The band gap is fixed at $E_g = 0.1$eV (gray shaded area) and the Lorenz function is related to the metallic limit $L_0 = 2.44 \times 10^{-8}$WΩK^{-2}.

Near the band edges the thermopower increases approximately as $S \sim \frac{-1}{\mu T}$. Thus L, as well as κ_{el}, minimizes and the minimum decreases with decreasing temperature, while shifting toward the middle of the gap (cf. Figure 1(a) in Ref. [141]). At a temperature of 100 K $\frac{L}{L_0}$ takes values of about 0.8 at the band edges. In the intrinsic regime $\frac{L}{L_0}$ and κ_{el} increase, whereas the thermopower is reduced due to bipolar contributions. In other words, this contribution to heat conductivity arises from the common electron and hole movement, transporting energy but not carrying any net charge [104]. According to Goldsmid [142] and Price [143] the maximum deviation of the Lorenz number from the metallic limit in the intrinsic regime holds to some extent $\frac{L}{L_0} = 1 + \frac{1}{2}\frac{m_{CB}m_{VB}}{(m_{CB}+m_{VB})^2}\left(\frac{E_g}{k_B T} + 4\right)^2$. Therefore, assuming a fixed charge carrier concentration, $\frac{L}{L_0}$ achieves very large values at small temperatures and/or large band gaps. Assuming the above approaches [142, 143], together with $m_{CB} = m_{VB}$ and $E_g = 0.1$eV one achieves $\frac{L}{L_0} \approx 9$ at room temperature for μ located deep in the gap. If $m_{VB} > m_{CB}$, as shown in Figure 10.10, the intrinsic regime $N_n = N_p$ and with that the maximal value of $\frac{L}{L_0}$ and κ_{el} at bipolar conduction shifts toward the CBM. With increasing m_{VB} and hence due to the enhanced electrical conductivity σ in the VB it is obvious that κ_{el} under hole doping will increase, too.

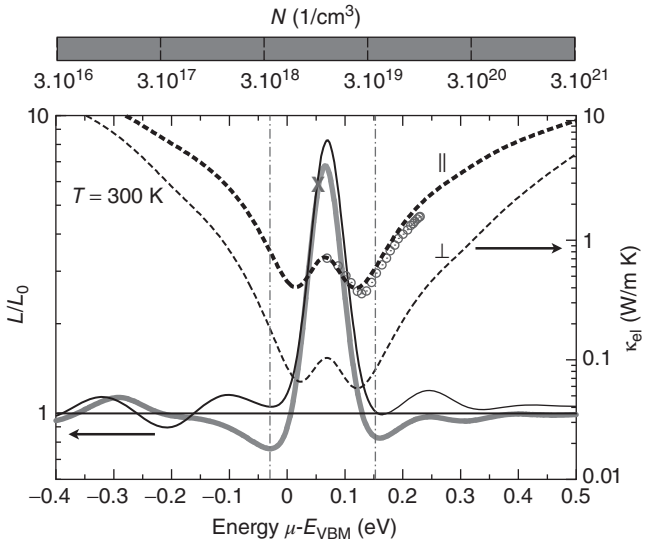

Figure 10.11 Lorenz function L (solid lines, ref. to left scale) and electronic contribution to the total thermal conductivity κ_{el} (dashed lines, ref. to the right scale) in dependence on the position of the chemical potential μ for bulk Bi_2Te_3 for the in-plane (thick lines) and cross-plane (thin lines) transport direction. The Lorenz function is given relative to the metallic limit $L_0 = 2.44 \times 10^{-8} W\Omega K^{-2}$. Superimposed onto the Lorenz function in the in-plane direction is a color code referring to the charge carrier concentration. The cross in the middle marks the change from hole to electron doping for smaller and larger values of μ, respectively. The temperature was fixed at 300 K. Thin vertical dash-dotted lines give the position of the chemical potential for a charge carrier concentration of $N = 3 \times 10^{19} cm^{-3}$ under n and p doping (right and left vertical line, respectively). The CBM is located at 0.105eV. Open circles show experimental values from Ref. [104] for $\kappa_{el,\parallel}$ for an *n*-type Bi_2Te_3 single crystal; adapted with permission from Ref. [141] (color online), Copyright (2012) APS.

Figure 10.11 shows the room temperature doping-dependent electronic part of the thermal conductivity, in the in-plane (thick dashed lines, right scale) and cross-plane direction (thin dashed lines, right scale), for bulk Bi_2Te_3, to offer insight into the principle dependencies. Furthermore, the Lorenz function defined via Equation 10.13 is shown for the in-plane (thick solid line, left scale) and cross-plane parts (thin solid line, left scale), respectively. As can be seen, κ_{el} minimizes for energies near the band edges. Here, at $N \approx 3 \times 10^{18} cm^{-3}$, the thermopower S maximizes at appropriate values for the electrical conductivity σ; hence, the second term in Equation 10.11 increases leading to small values for κ_{el}. At small intrinsic charge carrier concentrations, the chemical potential

shifts into the gap and the total thermopower is strongly reduced due to bipolar diffusion. This leads to an enhanced contribution to the electrical thermal conductivity at intrinsic charge carrier concentrations and is known as the bipolar thermodiffusion effect [104, 144, 145]. At charge carrier concentrations of $N = 3 \times 10^{19}\mathrm{cm}^{-3}$ we find $\kappa_{\mathrm{el}\parallel}$ to be about $0.6 - 0.8\,\mathrm{W/mK}$ for n/p-type bulk Bi_2Te_3, in very good agreement with experimental (cf. open circles in Figure 10.11) and theoretical results [20, 27, 142]. The cross-plane component of κ_{el} is substantially smaller, especially for n-type conduction, reflecting here the electrical conductivity anisotropy discussed earlier. The bipolar thermodiffusion effect is furthermore responsible for the suppression of the Lorenz function to values below the metallic limit L_0 ($L_0 = 2.44 \times 10^{-8}\mathrm{W\Omega K}^{-2}$) for values of the chemical potential near the band edges (cf. Figure 10.11 solid lines, left scale). At optimal charge carrier concentrations of $N = 3 \times 10^{19}\mathrm{cm}^{-3}$, the in-plane Lorenz numbers reach minimal values of $L_\parallel \approx 0.7L_0$ under hole doping (left dashed dotted vertical line) and $L_\parallel \approx 0.8L_0$ under electron doping (right dashed dotted vertical line). The cross-plane Lorenz function $L_\perp$ is approximately L_0 at this level of p- and n-type doping. Reaching the intrinsic doping regime the Lorenz function reaches substantially large values of $L_\parallel \approx 6.5L_0$ and $L_\perp \approx 8L_0$. Such a behavior has been already described in literature [27, 146] and might strongly influence the determination of the thermal conductivity. The Lorenz number is generally used to separate κ_{el} and κ_{ph}. At typical charge carrier concentrations applying the metallic value L_0 to determine the lattice thermal conductivity could lead to an overestimation of the electronic thermal conductivity, and consequently to underestimation of the lattice contribution. In the worst case, this can even result in non-physical negative values for κ_{ph} [147]. The Lorenz function of thermoelectric heterostructures can show further anomalies, which are discussed in detail in Ref. [141].

10.3.5 Phonons

The phonon dispersion (cf. Figure 10.12 (a)) and the corresponding phonon density of states (PDOS) have been calculated using a plane wave code (VASP[148, 149]) and the phonon Green function method, respectively. Accurate force calculations for Bi_2Te_3 supercells of 40 atoms have been performed to obtain the dynamical matrix and thus the phonon frequencies and the eigenvectors of the vibrational modes.

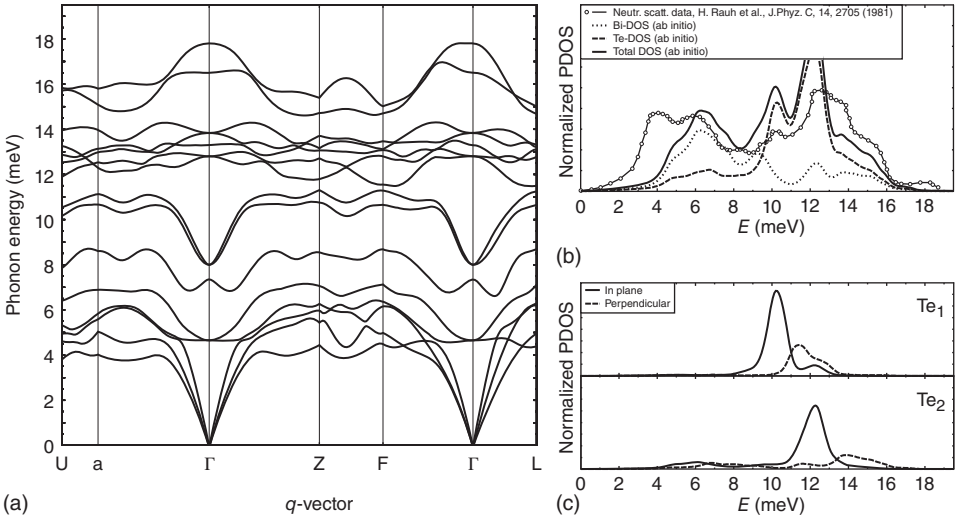

Figure 10.12 (a) Phonon dispersion of bulk Bi_2Te_3 obtained by a DFT supercell calculation. (b) Partial (dashed lines) and total phonon DOS of bulk Bi_2Te_3. Circles represent the corresponding neutron scattering measurements. (c) Directionally and spatially resolved phonon DOS for the two inequivalent Te sites. Straight lines show the in-plane components of the PDOS and dashed lines show the component parallel to *z* direction. The theoretical data in (b) and (c) have been convoluted with a Gaussian for better comparability with the measured curve.

Figure 10.12 (b) shows the calculated (solid line) and measured (circles, [150]) total PDOS of bulk Bi_2Te_3. The theoretical data have been convoluted with a Gaussian of full width 1.5 meV (experimental resolution) for better comparability. The overall correspondence between theory and experiment is quite good, with the exception of the acoustic bandwidth being overestimated by the calculations. The main peaks above 7 meV are in good agreement. Compared to other experimental methods, namely, ultrasonic studies [151] and recent synchrotron radiation measurements by Bessas *et al.* [152], even the acoustic branch is in good agreement with experiments. The dashed lines in (b) show the element-resolved partial PDOS of Bi and Te, respectively. Clearly, the locally resolved contributions to the acoustic branches and the lower optical modes below 10 meV are dominated by Bi, whereas the higher parts of the spectrum are dominated by Te oscillations. A view on the directional PDOS provides more insight into the main components of the optical frequencies. As example, Figure 10.12 (c) shows the in-plane and out-of plane components of the

partial PDOS of the Te_1 as well as the Te_2 site. The peaks of the PDOS at 10 meV and 12 meV mainly originate from the respective transverse and longitudinal oscillations of these atoms perpendicular to the *c* axis. In particular, the directional PDOS of Te_2 reflects the strong bonding within the Te layers, compared to the relatively weak interplanar forces at the van der Waals gap.

The presented methods help calculate accurate vibrational modes for Bi_2Te_2 from first principles, which are in good agreement with experimental data. However, it stays a challenge to evaluate the phonon-phonon coupling matrices and relaxation times necessary for obtaining the ab-initio lattice thermal conductivity.

10.4 Summary

The thermoelectric transport properties of bulk Bi_2Te_3 and Bi_2Te_3/Sb_2Te_3 superlattices are analyzed by means of first principles calculations and semiclassical Boltzmann transport theory. The anisotropy of the thermoelectric transport under electron and hole-doping is discussed in detail for different superlattice periods at various temperature and charge carrier concentrations. For bulk Bi_2Te_3 the power factor is found to decrease under applied in-plane strain. With the thermoelectric transport properties of bulk Sb_2Te_3 being robust under applied strain, a substrate favoring Bi_2Te_3 should be chosen when growing Bi_2Te_3/Sb_2Te_3 superlattices. A clear preference for thermoelectric transport under hole-doping, as well as for the in-plane transport direction is found for all superlattice periods. At hole-doping the electrical transport anisotropies remain bulk-like for all investigated systems, while under electron-doping quantum confinement leads to strong suppression of the cross-plane thermoelectric transport at several superlattice periods. In addition, insights on the Lorenz function, the electronic contribution to the thermal conductivity, and the resulting figure of merit are given. As no reduction in the electrical transport anisotropies compared to bulk can be manifested theoretically, values of ZT around unity at room temperature for the most efficient Bi_2Te_3/Sb_2Te_3 superlattices are found. The presented results on the vibronic structure of Bi_2Te_3 are in excellent agreement with recent synchrotron radiation measurements and encourage the possibility of engineering a low thermal conductivity material by means of first principles calculations.

References

1. Snyder, G.J. and Toberer, E.S. (2008) Complex thermoelectric materials. *Nat. Mater.*, **7** (2), 105–114, doi: 10.1038/nmat2090.
2. Vineis, C.J., Shakouri, A., Majumdar, A., and Kanatzidis, M.G. (2010) Nanostructured thermoelectrics: big efficiency gains from small features. *Adv. Mater.*, **22** (36): 3970–3980.
3. Wright, D.A. (1958) Thermoelectric properties of bismuth telluride and its alloys Nature. **181** (4612), 834, doi: 10.1038/181834a0.
4. Caillat, T., Carle, M., Pierrat, P., Scherrer, H., and Scherrer, S. (1992) Thermoelectric properties of $(Bi_xSb_{1-x})_2Te_3$ single crystal solid solutions grown by the THM method. *J. Phys. Chem. Solids*, **53** (8), 1121–1129, doi: 10.1016/0022-3697(92)90087-T.
5. Poudel, B., Hao, Q., Ma, Y., Lan, Y., Minnich, A., Yu, B., Yan, X., Wang, D., Muto, A., and Vashaee, D. (2008) High-thermoelectric performance of nanostructured bismuth antimony telluride bulk alloys. *Science*, **320** (5876), 634, doi: 10.1126/science.1156446.
6. Slack, G.A. (1995) *New Materials and Performance Limits for Thermoelectric Cooling*, Chapter 34, CRC Press, Boca Raton, FL.
7. Chen, G. (1998) Thermal conductivity and ballistic-phonon transport in the cross-plane direction of superlattices. *Phys. Rev. B*, **57** (23), 14958, doi: 10.1103/PhysRevB.57.14958.
8. Venkatasubramanian, R. (2000) Lattice thermal conductivity reduction and phonon localizationlike behavior in superlattice structures. *Phys. Rev. B*, **61** (4), 3091–3097, doi: 10.1103/PhysRevB.61.3091.
9. Koga, T., Sun, X., Cronin, S.B., and Dresselhaus, M.S. (1999) Carrier pocket engineering to design superior thermoelectric materials using superlattice structures. 18th International Conference on Thermoelectrics, pp. 378–381.
10. Koga, T., Sun, X., Cronin, S.B., and Dresselhaus, M.S. (1999) Carrier pocket engineering applied to strained Si/Ge superlattices to design useful thermoelectric materials. *Appl. Phys. Lett.*, **75**, 2438, doi: 10.1063/1.125040.
11. Koga, T., Harman, T., Cronin, S., and Dresselhaus, M.S. (1999) Mechanism of the enhanced thermoelectric power in (111)-oriented n-type $PbTe/Pb_{1-x}Eu_xTe$. *Phys. Rev. B*, **60** (20), 14286, doi: 10.1103/PhysRevB.60.14286.
12. Koga, T., Cronin, S., Dresselhaus, M., and Liu, J. (2000) Experimental proof-of-principle investigation of enhanced ZT in (001) oriented Si/Ge superlattices. *Appl. Phys. Lett.*, **77** (10), 1490, doi: 10.1063/1.1308271.
13. Böttner, H., Chen, G., and Venkatasubramanian, R. (2006) Aspects of thin-film superlattice thermoelectric materials, devices, and applications. *MRS Bull.*, **31** (3), 211, doi: 10.1557/mrs2006.47.
14. Venkatasubramanian, R., Colpitts, T., O'Quinn, B., Liu, S., El-Masry, N., and Lamvik, M. (1999) Low-temperature organometallic epitaxy and its application to superlattice structures in thermoelectrics. *Appl. Phys. Lett.*, **75** (8), 1104–1106, doi: 10.1063/1.124610.
15. Venkatasubramanian, R., Siivola, E., and Colpitts, T. (2001) Thin-film thermoelectric devices with high room-temperature figures of merit. *Nature*, **413**, 597, doi: 10.1038/35098012.
16. Beyer, H., Nurnus, J., Böttner, H., Lambrecht, A., Wagner, E., and Bauer, G. (2002) High thermoelectric figure of merit ZT in PbTe and Bi_2Te_3-based superlattices by a reduction of the thermal conductivity. *Physica E*, **13** (2-4), 965–968, doi: 10.1016/S1386-9477(02)00246-1.
17. Böttner, H., Nurnus, J., Gavrikov, A., and Kuhner, G. (2004) New thermoelectric components using microsystem technologies. *J. Microelectromech. Syst.*, **13** (3), 414.
18. König, J., Winkler, M., Buller, S., Bensch, W., Schürmann, U., Kienle, L., and Böttner, H. (2011) $Bi_2Te_3 - Sb_2Te_3$

superlattices grown by nanoalloying. *J. Electron. Mater.*, **40** (5), 1266, doi: 10.1007/s11664-011-1578-0.

19. Liao, C.-N., Chang, C.-Y., and Chu, H.-S. (2010) Thermoelectric properties of electrically stressed Sb/Bi–Sb–Te multilayered films. *J. Appl. Phys.*, **107** (6), 066103.
20. Peranio, N., Eibl, O., and Nurnus, J. (2006) Structural and thermoelectric properties of epitaxially grown bi2te3 thin films and superlattices. *J. Appl. Phys.*, **100** (11), 114306.
21. Touzelbaev, M.N., Zhou, P., Venkatasubramanian, R., and Goodson, K.E. (2010) Thermal characterization of bi2te3/sb2te3 superlattices. *J. Appl. Phys.*, **90** (2), 763.
22. Peranio, N., Winkler, M., Aabdin, Z., König, J., Böttner, H., and Eibl, O. (2011) Room temperature mbe deposition of bi2te3 and sb2te3 thin films with low charge carrier densities. *Phys. Status Solidi A*, **209** (2), 289–293.
23. Winkler, M., Liu, X., König, J.D., Kirste, L., Böttner, H., Bensch, W., and Kienle, L. (2012) Sputtered p-type sb 2 te 3/(bi, sb) 2 te 3 soft superlattices created by nanoalloying. *J. Electron. Mater.*, **41** (6), 1322–1331.
24. Scheidemantel, T.J., Ambrosch-Draxl, C., Thonhauser, T., Badding, J.V., and Sofo, J.O. (2003) Transport coefficients from first-principles calculations. *Phys. Rev. B*, **68** (12), 125210.
25. Thonhauser, T., Scheidemantel, T., Sofo, J.O., Badding, J., and Mahan, G. (2003) Thermoelectric properties of sb2te3 under pressure and uniaxial stress. *Phys. Rev. B*, **68** (8), 085201.
26. Wang, G. and Cagin, T. (2007) Electronic structure of the thermoelectric materials Bi_2Te_3 and Sb_2Te_3 from first-principles calculations. *Phys. Rev. B*, **76** (7), 075201.
27. Huang, B. and Kaviany, M. (2008) Ab initio and molecular dynamics predictions for electron and phonon transport in bismuth …. *Phys. Rev. B*, **77** (12), 125209.
28. Wang, G. and Cagin, T. (2006) Investigation of effective mass of carriers in bi2te3/sb2te3 superlattices via electronic structure studies on its component crystals. *Appl. Phys. Lett.*, **89** (15), 152101.
29. Park, M.S., Song, J.-H., Medvedeva, J.E., Kim, M., Kim, G., and Freeman, A.J. (2010) Electronic structure and volume effect on thermoelectric transport in p -type bi and sb tellurides. *Phys. Rev. B*, **81** (15), 155211.
30. Hinsche, N., Yavorsky, B., Mertig, I., and Zahn, P. (2011) Influence of strain on anisotropic thermoelectric transport in Bi_2Te_3 and Sb_2Te_3. *Phys. Rev. B*, **84** (16), 165214.
31. Li, H., Bilc, D., and Mahanti, S.D. (2004) Theoretical study of electronic structures of bi2te3 /sb2te3 superlattices. *Mater. Res. Soc. Symp. Proc.*, **793**, 837.
32. Mahanti, S.D., Larson, P.M., and Li, H. (2003) *Electronic Structure of Complex Bismuth Chalcogenide Systems*, Kluwer Academic/Plenum Publishers, New York, p. 227.
33. Hicks, L. and Dresselhaus, M. (1993) Effect of quantum-well structures on the thermoelectric figure of merit. *Phys. Rev. B*, **47** (19), 12727–12731, doi: 10.1103/PhysRevB.47.12727.
34. Hicks, L.D., Harman, T.C., and Dresselhaus, M.S. (1993) Use of quantum-well superlattices to obtain a high figure of merit from nonconventional thermoelectric materials. *Appl. Phys. Lett.*, **63** (23), 3230–3232, doi: 10.1063/1.110207.
35. Shakouri, A. (2011) Recent developments in semiconductor thermoelectric physics and materials. *Annu. Rev. Mater. Res.*, **41**, 399–431, doi: 10.1146/annurev-matsci-062910-100445.
36. Dresselhaus, M.S., Dresselhaus, G., Sun, X., Zhang, Z., Cronin, S.B., and Koga, T. (1999) Low-dimensional thermoelectric materials. *Phys. Solid State*, **41** (5), 679–682, doi: 10.1134/1.1130849.
37. Broido, D. and Reinecke, T. (1995) Effect of superlattice structure on the thermoelectric figure of merit. *Phys.*

Rev. B, **51** (19), 13797–13800, doi: 10.1103/PhysRevB.51.13797.

38. Broido, D.A. and Reinecke, T.L. (1995) Thermoelectric figure of merit of quantum wire superlattices. *Appl. Phys. Lett.*, **67** (1), 100–102, doi: 10.1063/1.115495.
39. Cornett, J.E. and Rabin, O. (2011) Thermoelectric figure of merit calculations for semiconducting nanowires. *Appl. Phys. Lett.*, **98** (18), 182104, doi: 10.1063/1.3585659.
40. Hicks, L., Harman, T., Sun, X., and Dresselhaus, M. (1996) Experimental study of the effect of quantum-well structures on the thermoelectric figure of merit. *Phys. Rev. B*, **53** (16), R10493–R10496, doi: 10.1103/PhysRevB.53.R10493.
41. Harman, T.C., Taylor, P.J., Spears, D.L., and Walsh, M.P. (2000) Thermoelectric quantum-dot superlattices with high ZT. *J. Electron. Mater.*, **29** (1), L1–L2, doi: 10.1007/s11664-000-0117-1.
42. Harman, T., Taylor, P., Walsh, M., and LaForge, B. (2002) Quantum dot superlattice thermoelectric materials and devices. *Science*, **297** (5590), 2229, doi: 10.1126/science.1072886.
43. Harman, T.C., Walsh, M.P., Laforge, B.E., and Turner, G.W. (2005) Nanostructured thermoelectric materials. *J. Electron. Mater.*, **34** (5), L19–L22, doi: 10.1007/s11664-005-0083-8.
44. Ohta, H. (2007) Thermoelectrics based on strontium titanate. *Mater. Today*, **10** (10), 44–49, doi: 10.1016/S1369-7021(07)70244-4.
45. Ohta, H., Kim, S.W., Mune, Y., Mizoguchi, T., Nomura, K., Ohta, S., Nomura, T., Nakanishi, Y., Ikuhara, Y., Hirano, M., Hosono, H., and Koumoto, K. (2007) Giant thermoelectric Seebeck coefficient of a two-dimensional electron gas in $SrTiO_3$. *Nat. Mater.*, **6** (2), 129, doi: 10.1038/nmat1821.
46. Ohta, H., Mune, Y., Koumoto, K., Mizoguchi, T., and Ikuhara, Y. (2008) Critical thickness for giant thermoelectric Seebeck coefficient of 2DEG confined in $SrTiO_3/SrTi_{0.8}Nb_{0.2}O_3$ superlattices. *Thin Solid Films*, **516** (17), 5916–5920, doi: 10.1016/j.tsf.2007.10.034.
47. Jalan, B. and Stemmer, S. (2010) Large Seebeck coefficients and thermoelectric power factor of La-doped $SrTiO_3$ thin films. *Appl. Phys. Lett.*, **97** (4), 3, doi: 10.1063/1.3471398.
48. Vineis, C.J., Harman, T.C., Calawa, S.D., Walsh, M.P., Reeder, R.E., Singh, R., and Shakouri, A. (2008) Carrier concentration and temperature dependence of the electronic transport properties of epitaxial PbTe and PbTe/PbSe nanodot superlattices. *Phys. Rev. B*, **77** (23), 235202, doi: 10.1103/PhysRevB.77.235202.
49. Kim, R., Datta, S., and Lundstrom, M.S. (2009) Influence of dimensionality on thermoelectric device performance. *J. Appl. Phys.*, **105** (3), 034506, doi: 10.1063/1.3074347.
50. Li, D., Wu, Y., Kim, P., Shi, L., Yang, P., and Majumdar, A. (2003) Thermal conductivity of individual silicon nanowires. *Appl. Phys. Lett.*, **83** (14), 2934–2936, doi: 10.1063/1.1616981.
51. Zhou, J., Jin, C., Seol, J.H., Li, X., and Shi, L. (2005) Thermoelectric properties of individual electrodeposited bismuth telluride nanowires. *Appl. Phys. Lett.*, **87** (13), 133109, doi: 10.1063/1.2058217.
52. Boukai, A.I., Bunimovich, Y., Tahir-Kheli, J., Yu, J.K., Goddard, W.A. III, and Heath, J.R. (2008) Silicon nanowires as efficient thermoelectric materials. *Nature*, **451** (7175), 168–171, doi: 10.1038/nature06458.
53. Chen, R., Hochbaum, A.I., Murphy, P., Moore, J., Yang, P., and Majumdar, A. (2008) Thermal conductance of thin silicon nanowires. *Phys. Rev. Lett.*, **101** (10), 105501, doi: 10.1103/PhysRevLett.101.105501.
54. Hochbaum, A., Chen, R., Delgado, R., and Liang, W. (2008) Enhanced thermoelectric performance of rough silicon nanowires. *Nature*, **451** (7175), 163, doi: 10.1038/nature06381.
55. Tai, G., Zhou, B., and Guo, W. (2008) Structural characterization and thermoelectric transport properties of

uniform single-crystalline lead telluride nanowires. *J. Phys. Chem. C*, **112** (30), 11314–11318, doi: 10.1021/jp8041318.

56. Yang, R.B., Bachmann, J., Pippel, E., Berger, A., Woltersdorf, J., Gösele, U., and Nielsch, K. (2009) Pulsed vapor-liquid-solid growth of antimony selenide and antimony sulfide nanowires. *Adv. Mater.*, **21** (31), 3170–3174, doi: 10.1002/adma.200803436.

57. Lin, Y.-M. and Dresselhaus, M. (2003) Thermoelectric properties of superlattice nanowires. *Phys. Rev. B*, **68** (7), 075304, doi: 10.1103/PhysRevB.68.075304.

58. Weber, L., Lehr, M., and Gmelin, E. (1992) Reduction of the thermopower in semiconducting point contacts. *Phys. Rev. B*, **46** (15), 9511–9514, doi: 10.1103/PhysRevB.46.9511.

59. Mahan, G. and Sofo, J.O. (1996) The best thermoelectric. *Proc. Natl. Acad. Sci. U.S.A.*, **93** (15), 7436, *www.pnas.org/content/93/15/7436.abstract* (accessed 28 October 2014).

60. Heremans, J.P., Jovovic, V., Toberer, E.S., Saramat, A., Kurosaki, K., Charoenphakdee, A., Yamanaka, S., and Snyder, G.J. (2008) Enhancement of thermoelectric efficiency in PbTe by distortion of the electronic density of states. *Science*, **321** (5888), 554, doi: 10.1126/science.1159725.

61. Jaworski, C.M., Kulbachinskii, V., and Heremans, J.P. (2009) Resonant level formed by tin in Bi_2Te_3 and the enhancement of room-temperature thermoelectric power. *Phys. Rev. B*, **80** (23), 233201, doi: 10.1103/PhysRevB.80.233201.

62. Lee, J.-H., Wu, J., and Grossman, J.C. (2010) Enhancing the thermoelectric power factor with highly mismatched isoelectronic doping. *Phys. Rev. Lett.*, **104** (1), 016602, doi: 10.1103/PhysRevLett.104.016602.

63. König, J., Nielsen, M., Gao, Y.-B., Winkler, M., Jacquot, A., Böttner, H., and Heremans, J. (2011) Titanium forms a resonant level in the conduction band of PbTe. *Phys. Rev. B*, **84** (20), 205126, doi: 10.1103/PhysRevB.84.205126.

64. Ioffe, A.F. (1957) *Semiconductor Thermoelements, and Thermoelectric Cooling*, Infosearch, London, ISBN: 0850860393.

65. Slack, G.A. (1995) *CRC Handbook of Thermoelectrics*, Chapter 34, CRC Press, Boca Raton, FL, p. 701, ISBN: 0849301467.

66. Slack, G.A. (1979) The thermal conductivity of nonmetallic crystals, in *Solid State Physics*, vol. **34**, Academic Press, New York, pp. 1–71, doi: 10.1016/S0081-1947(08)60359-8.

67. Cahill, D. and Pohl, R. (1987) Thermal conductivity of amorphous solids above the plateau. *Phys. Rev. B*, **35** (8), 4067–4073, doi: 10.1103/PhysRevB.35.4067.

68. Nolas, G.S., Morelli, D.T., and Tritt, T.M. (1999) Skutterudites: a phonon-glass-electron crystal approach to advanced thermoelectric energy conversion applications. *Annu. Rev. Mater. Sci.*, **29**, 89–116, doi: 10.1146/annurev.matsci.29.1.89.

69. Nolas, G.S., Slack, G.A., Morelli, D.T., Tritt, T.M., and Ehrlich, A.C. (1996) The effect of rare-earth filling on the lattice thermal conductivity of skutterudites. *J. Appl. Phys.*, **79** (8), 4002–4008, doi: 10.1063/1.361828.

70. Nolas, G.S., Cohn, J.L., and Slack, G.A. (1998) Effect of partial void filling on the lattice thermal conductivity of skutterudites. *Phys. Rev. B*, **58** (1), 164, doi: 10.1103/PhysRevB.58.164.

71. Shi, X., Kong, H., Li, C.P., Uher, C., Yang, J., Salvador, J.R., Wang, H., Chen, L., and Zhang, W. (2008) Low thermal conductivity and high thermoelectric figure of merit in n-type BaYbCoSb double-filled skutterudites. *Appl. Phys. Lett.*, **92**, 182101, doi: 10.1063/1.2920210.

72. Vining, C.B. (2008) Thermoelectrics: half-full glasses. *Nat. Mater.*, **7** (10), 765, doi: 10.1038/nmat2271.

73. Nolas, G.S., Cohn, J.L., Slack, G.A., and Schujman, S.B. (1998) Semiconducting Ge clathrates: promising candidates for

thermoelectric applications. *Appl. Phys. Lett.*, **73** (2), 178–180, doi: 10.1063/1.121747.

74. Dong, J., Sankey, O., and Myles, C. (2001) Theoretical study of the lattice thermal conductivity in Ge framework semiconductors. *Phys. Rev. Lett.*, **86** (11), 2361, doi: 10.1103/PhysRevLett.86.2361.
75. Bentien, A., Christensen, M., Bryan, J., Sanchez, A., Paschen, S., Steglich, F., Stucky, G., and Iversen, B. (2004) Thermal conductivity of thermoelectric clathrates. *Phys. Rev. B*, **69** (4), 045107, doi: 10.1103/PhysRevB.69.045107.
76. Shi, X., Yang, J., Bai, S., Yang, J., Wang, H., Chi, M., Salvador, J.R., Zhang, W., Chen, L., and Wong-Ng, W. (2010) On the design of high-efficiency thermoelectric clathrates through a systematic cross-substitution of framework elements. *Adv. Funct. Mater.*, **20** (5), 755–763, doi: 10.1002/adfm.200901817.
77. Toberer, E.S., Cox, C.A., Brown, S.R., Ikeda, T., May, A.F., Kauzlarich, S.M., and Snyder, G.J. (2008) Traversing the metal-insulator transition in a zintl phase: rational enhancement of thermoelectric efficiency in $Yb_{14}Mn_{1-x}Al_xSb_{11}$. *Adv. Funct. Mater.*, **18** (18), 2795–2800, doi: 10.1002/adfm.200800298.
78. Toberer, E.S., May, A.F., and Snyder, G.J. (2009) Zintl chemistry for designing high efficiency thermoelectric materials. *Chem. Mater.*, **22** (3), 624–634, doi: 10.1021/cm901956r.
79. Zevalkink, A., Zeier, W.G., Pomrehn, G., Schechtel, E., Tremel, W., and Snyder, G.J. (2012) Thermoelectric properties of Sr_3GaSb_3—a chain-forming Zintl compound. *Energy Environ. Sci.*, **5** (10), 9121–9128, doi: 10.1039/C2EE22378C.
80. Roufosse, M. and Klemens, P. (1973) Thermal conductivity of complex dielectric crystals. *Phys. Rev. B*, **7** (12), 5379–5386, doi: 10.1103/PhysRevB.7.5379.
81. Tiwari, M.D. (1978) Contribution of optical phonons in lattice thermal conductivity of NaCl. *Il Nuovo Cimento B*, **48** (1), 102–108, doi: 10.1007/BF02748652.
82. Zou, J. and Balandin, A. (2001) Phonon heat conduction in a semiconductor nanowire. *J. Appl. Phys.*, **89** (5), 2932–2938, doi: 10.1063/1.1345515.
83. Liu, H., Shi, X., Xu, F., Zhang, L., Zhang, W., Chen, L., Li, Q., Uher, C., Day, T., and Snyder, G.J. (2012) Copper ion liquid-like thermoelectrics. *Nat. Mater.*, **11** (5), 422, doi: 10.1038/nmat3273.
84. Venkatasubramanian, R., Colpitts, T., Watko, E., Lamvik, M., and El-Masry, N. (1997) MOCVD of Bi_2Te_3, Sb_2Te_3 and their superlattice structures for thin-film thermoelectric applications. *J. Cryst. Growth*, **170** (1-4), 817–821, doi: 10.1016/S0022-0248(96)00656-2.
85. Touzelbaev, M.N., Zhou, P., Venkatasubramanian, R., and Goodson, K.E. (2001) Thermal characterization of Bi_2Te_3/Sb_2Te_3 superlattices. *J. Appl. Phys.*, **90** (2), 763, doi: 10.1063/1.1374458.
86. Winkler, M., Liu, X., König, J.D., Kirste, L., Böttner, H., Bensch, W., and Kienle, L. (2011) Sputtered p-Type $Sb_2Te_3/(Bi,Sb)_2Te_3$ soft superlattices created by nanoalloying. *J. Electron. Mater.*, **41** (6), 1322, doi: 10.1007/s11664-011-1854-z.
87. Winkler, M., Liu, X., König, J.D., Buller, S., Schürmann, U., Kienle, L., Bensch, W., and Böttner, H. (2012) Electrical and structural properties of Bi_2Te_3 and Sb_2Te_3 thin films grown by the nanoalloying method with different deposition patterns and compositions. *J. Mater. Chem.*, **22** (22), 11323–11334, doi: 10.1039/c2jm30363a.
88. Venkatasubramanian, R., Colpitts, T., Watko, E., and Hutchby, J. (1996) Experimental evidence of high power factors and low thermal conductivity in Bi_2Te_3/Sb_2Te_3 superlattice thin-films. Proceedings of the 15th International Conference on Thermoelectrics, pp. 454–458, doi: 10.1109/ICT.1996.553526.
89. Venkatasubramanian, R. (1997) Bi_2Te_3/Sb_2Te_3 superlattice structures

for high-ZT thermoelectric cooling devices. Naval Research Reviews, Special Issue on Thermoelectric, *http://www.dtic.mil/get-tr-doc/pdf?AD=ADA327170*.

90. Lee, S., Cahill, D., and Venkatasubramanian, R. (1997) Thermal conductivity of Si–Ge superlattices. *Appl. Phys. Lett.*, **70** (22), 2957, doi: 10.1063/1.118755.
91. Borca-Tasciuc, T. (2000) Thermal conductivity of symmetrically strained Si/Ge superlattices. *Superlattices Microstruct.*, **28** (3), 199–206, doi: 10.1006/spmi.2000.0900.
92. Yang, B., Liu, J., Wang, K., and Chen, G. (2001) Characterization of cross-plane thermoelectric properties of Si/Ge superlattices. Proceedings of the 10th International Conference on Thermoelectrics, pp. 344–347, doi: 10.1109/ICT.2001.979902.
93. Beyer, H., Nurnus, J., Böttner, H., Lambrecht, A., Roch, T., and Bauer, G. (2002) PbTe based superlattice structures with high thermoelectric efficiency. *Appl. Phys. Lett.*, **80** (7), 1216, doi: 10.1063/1.1448388.
94. Jeffers, J.D., Namjou, K., Cai, Z., McCann, P.J., and Olona, L. (2011) Cross-plane thermal conductivity of a PbSnSe/PbSe superlattice material. *Appl. Phys. Lett.*, **99** (4), 041903, doi: 10.1063/1.3615797.
95. Cho, S., Kim, Y., Youn, S., DiVenere, A., and Wong, G. (2001) Artificially ordered Bi/Sb superlattice alloys: fabrication and transport properties. *Phys. Rev. B*, **64** (23), 235330, doi: 10.1103/PhysRevB.64.235330.
96. Caylor, J., Sander, M., Stacy, A., Harper, J., Gronsky, R., and Sands, T. (2001) Epitaxial growth of skutterudite $CoSb_3$ thin films on (001) InSb by pulsed laser deposition. *J. Mater. Res.*, **16** (9), 2467, doi: 10.1557/JMR.2001.0337.
97. Chakraborty, S., Kleint, C.A., Heinrich, A., Schneider, C.M., Schumann, J., Falke, M., and Teichert, S. (2003) Thermal conductivity in strain symmetrized Si/Ge superlattices on Si (111). *Appl. Phys. Lett.*, **83**, 4184, doi: 10.1063/1.1628819.
98. Huxtable, S., Abramson, A., and Tien, C. (2002) Thermal conductivity of Si/SiGe and SiGe/SiGe superlattices. *Appl. Phys. Lett.*, **80** (10), 1737, doi: 10.1063/1.1455693.
99. Ezzahri, Y., Grauby, S., Rampnoux, J., Michel, H., Pernot, G., Claeys, W., Dilhaire, S., Rossignol, C., Zeng, G., and Shakouri, A. (2007) Coherent phonons in Si/SiGe superlattices. *Phys. Rev. B*, **75** (19), 195309, doi: 10.1103/PhysRevB.75.195309.
100. Hyldgaard, P. and Mahan, G.D. (1997) Phonon superlattice transport. *Phys. Rev. B: Condens. Matter*, **56** (17), 10754–10757, doi: 10.1103/PhysRevB.56.10754.
101. Tamura, S., Tanaka, Y., and Maris, H.J. (1999) Phonon group velocity and thermal conduction in superlattices. *Phys. Rev. B*, **60** (4), 2627, doi: 10.1103/PhysRevB.60.2627.
102. Ziman, J.M. (1960) *Electrons and Phonons: The Theory of Transport Phenomena in Solids*, Clarendon Press, Oxford, ISBN: 0198507798.
103. Mertig, I. (1999) Transport properties of dilute alloys. *Rep. Prog. Phys.*, **62**, 237–276, doi: 10.1088/0034-4885/62/2/004.
104. Goldsmid, H.J. (1965) Transport effects in semi-metals and narrow-gap semiconductors. *Adv. Phys.*, **14** (55), 273, doi: 10.1080/00018736500101061.
105. Nolas, G.S. and Goldsmid, H.J. (2004) *Thermal Conductivity of Semiconductors*, Chapter 1.4, Kluwer Academic, New York.
106. Callaway, J. (1959) Model for lattice thermal conductivity at low temperatures. *Phys. Rev.*, **113** (4), 1046–1051, doi: 10.1103/PhysRev.113.1046.
107. Guyer, R. and Krumhansl, J. (1966) Solution of the linearized phonon boltzmann equation. *Phys. Rev.*, **148** (2), 766–778, doi: 10.1103/PhysRev.148.766.
108. Smith, H. and Jensen, H.H. (1989) *Transport Phenomena*, Clarendon Press, Oxford, ISBN: 0198519850.

109. Madelung, O., Schulz, M., and Weiss, H. (eds) (1998) *Landolt-Börnstein New Series, group III/41C*, Springer-Verlag, Berlin.

110. Yavorsky, B.Y., Hinsche, N., Mertig, I., and Zahn, P. (2011) Electronic structure and transport anisotropy of Bi_2Te_3 and Sb_2Te_3. *Phys. Rev. B*, **84** (16), 165208.

111. Hinsche, N.F., Yavorsky, B.Y., Gradhand, M., Czerner, M., Winkler, M., König, J., Böttner, H., Mertig, I., and Zahn, P. (2012) Thermoelectric transport in Bi_2Te_3/Sb_2Te_3 superlattices. *Phys. Rev. B*, **86**, 085323.

112. Delves, R., Bowley, A., and Hazelden, D. (1961) Anisotropy of the electrical conductivity in bismuth telluride. *Proc. Phys. Soc.*, **78** (5), 838, doi: 10.1088/0370-1328/78/5/329.

113. Goldsmid, H.J., Sheard, A.R., and Wright, D.A. (1958) The performance of bismuth telluride thermojunctions. *Br. J. Appl. Phys.*, **9** (9), 365, doi: 10.1088/0508-3443/9/9/306.

114. Langhammer, H.T., Stordeur, M., Sobotta, H., and Riede, V. (1982) Optical and electrical investigations of the anisotropy of sb2te3 single crystals. *Phys. Status Solidi B*, **109** (2), 673–681.

115. Müller, E. (1998) *Bandstruktur und Ladungsträgerstreuung in p-leitenden* $(Bi_{1-x}Sb_x)_2Te_3$*-Mischkristallen*, VDI Verlag, Düsseldorf.

116. Rowe, D.M. (ed.) (1995) *CRC Handbook of Thermoelectrics*, CRC Press, London.

117. Cho, S., Kim, Y., Divenere, A., Wong, G.K., Ketterson, J.B., and Meyer, J.R. (1999) Antisite defects of bi2te3 thin films. *Appl. Phys. Lett.*, **75** (10), 1401.

118. Zahn, P., Yavorsky, B.Y., Hinsche, N.F., and Mertig, I. (2011) Bi_2Te_3: implications of the rhombohedral k-space texture on the evaluation of the in-plane/out-of-plane conductivity anisotropy. *J. Phys. Condens. Matter*, **23**, 505504.

119. Hinsche, N.F., Yavorsky, B.Y., Mertig, I., and Zahn, P. (2011) Influence of strain on the anisotropic thermoelectric transport properties of Bi_2Te_3 and Sb_2Te_3. *Phys. Rev. B*, **84**, 165214.

120. Kaibe, H. (1989) Anisotropic galvanomagnetic and thermoelectric properties of n-type Bi_2Te_3 single crystal with the composition of a useful thermoelectric cooling material. *J. Phys. Chem. Solids*, **50** (9), 945–950, doi: 10.1016/0022-3697(89)90045-0.

121. Jeon, H.W., Ha, H.P., Hyun, D.B., and Shim, J.D. (1991) Electrical and thermoelectrical properties of undoped bi2te3-sb2te3 and bi2te3-sb2te3-sb2se3 single crystals. *J. Phys. Chem. Solids*, **52** (4), 579–585.

122. Stordeur, M. and Kühnberger, W. (1975) Nichtparabolizität des Valenzbandes von Bi_2Te_3 gefolgert aus transporteigenschaften. *Phys. Status Solidi B*, **69** (2), 377–387, doi: 10.1002/pssb.2220690208.

123. Zhitinskaya, M.K., Kaidanov, V.I., and Kondratev, V.P. (1976) Anisotropy of thermoelectric-power in bismuth telluride single-crystals. *Sov. Phys. Semicond.*, **10** (11), 1300.

124. Stordeur, M. and Heiliger, W. (1976) Anisotropy of the thermopower of *p*-Sb_2Te_3. *Phys. Status Solidi B*, **78** (2), K103–K106, doi: 10.1002/pssb.2220780255.

125. Cutler, M. and Mott, N. (1969) Observation of Anderson localization in an electron gas. *Phys. Rev.*, **181** (3), 1336, doi: 10.1103/PhysRev.181.1336.

126. Simon, G. and Eichler, W. (1981) Galvanomagnetische und thermoelektrische transportuntersuchungen an sb2te3. *Phys. Status Solidi B*, **103**, 289.

127. Nurnus, J. (2001) Thermoelektrische Effekte in Übergittern und Multi-Quantentrog-Strukturen. PhD thesis. Albert-Ludwigs-Universität Freiburg.

128. Lehmann, G. and Taut, M. (1972) On the numerical calculation of the density of states and related properties. *Phys. Status Solidi B*, **54** (2), 469–477, doi: 10.1002/pssb.2220540211.

129. Mertig, I., Mrosan, E., and Ziesche, P. (1987) *Multiple Scattering Theory of Point Defects in Metals: Electronic Properties, Teubner-Texte zur Physik*, Band **11**, B. G. Teubner Verlagsgesellschaft, Leipzig, ISBN: 3322004406.

130. Sehr, R. (1962) The optical properties of p-type Bi_2Te_3/Sb_2Te_3 alloys between 2–15 microns. *J. Phys. Chem. Solids*, **23** (9), 1219–1224.
131. von Middendorff, A., Dietrich, K., and Landwehr, G. (1973) Shubnikov-de haas effect in p-type sb2 te3. *Solid State Commun.*, **13** (4), 443–446.
132. Zhang, H., Liu, C.X., Qi, X.L., Dai, X., Fang, Z., and Zhang, S.C. (2009) Topological insulators in Bi_2Se_3, Bi_2Te_3 and Sb_2Te_3 with a single Dirac cone on the surface. *Nat. Phys.*, **5** (6), 438–442, doi: 10.1038/NPHYS1270.
133. Mishra, S., Satpathy, S., and Jepsen, O. (1997) Electronic structure and thermoelectric properties of bismuth telluride and bismuth selenide. *J. Phys. Condens. Matter*, **9**, 461.
134. Youn, S.J. and Freeman, A.J. (2001) First-principles electronic structure and its relation to thermoelectric properties of Bi_2Te_3. *Phys. Rev. B*, **63** (8), 85112.
135. Larson, P. (2006) Effects of uniaxial and hydrostatic pressure on the valence band maximum in Sb_2Te_3: an electronic structure study. *Phys. Rev. B*, **74** (20), 205113, doi: 10.1103/PhysRevB.74.205113.
136. Sofo, J.O. and Mahan, G.D. (1994) Superlattices in thermoelectric applications. AIP Conference Proceedings, vol. **316**, 239.
137. Zahn, P., Binder, J., Mertig, I., Zeller, R., and Dederichs, P. (1998) Origin of giant magnetoresistance: bulk or interface scattering. *Phys. Rev. Lett.*, **80** (19), 4309–4312, doi: 10.1103/PhysRevLett.80.4309.
138. Peranio, N. (2008) Structural, chemical, and thermoelectric properties of Bi_2Te_3 Peltier materials: bulk, thin films, and superlattices. PhD thesis. Eberhard-Karls-Universität zu Tübingen.
139. Hase, M. and Tominaga, J. (2011) Thermal conductivity of gete/sb2te3 superlattices measured by coherent phonon spectroscopy. *Appl. Phys. Lett.*, **99** (3), 031902.
140. Pattamatta, A. and Madnia, C.K. (2009) Modeling heat transfer in bi2te3-sb2te3 nanostructures. *Int. J. Heat Mass Transfer*, **52** (3-4), 860–869.
141. Hinsche, N.F., Mertig, I., and Zahn, P. (2012) Lorenz function of Bi_2Te_3/Sb_2Te_3 superlattices. *J. Electron. Mater.*, doi: 10.1007/s11664-012-2279-z.
142. Goldsmid, H. (1956) The thermal conductivity of bismuth telluride. *Proc. Phys. Soc. London, Sect. B*, **69**, 203, doi: 10.1088/0370-1301/69/2/310.
143. Price, P.J. (1956) Anomalous lorenz numbers in mixed semiconductors. *Proc. Phys. Soc. London, Sect. B*, **69** (8), 851, doi: 10.1088/0370-1301/69/8/117.
144. Fröhlich, H. and Kittel, C. (1954) Remark on the paper by Prof. G. Busch. *Physica*, **3**, 1086–1086, doi: 10.1016/S0031-8914(54)80240-0.
145. Uher, C. and Goldsmid, H.J. (1974) Separation of electronic and lattice thermal-condcutivities in bismuth crystals. *Phys. Status Solidi B*, **65** (2), 765–772, doi: 10.1002/pssb.2220650237.
146. Chaput, L., Pécheur, P., Tobola, J., and Scherrer, H. (2005) Transport in doped skutterudites: Ab initio electronic structure calculations. *Phys. Rev. B*, **72** (8), 085126.
147. Sharp, J.W., Volckmann, E.H., and Goldsmid, H.J. (2001) The thermal conductivity of polycrystalline $Bi_{88}Sb_{12}$. *Phys. Status Solidi A*, **185** (2), 257–265, doi: 10.1002/1521-396X(200106)185:2<257::AID-PSSA257>3.0.CO;2-D.
148. Kresse, G. and Furthmüller, J. (1996) *Phys. Rev. B*, **54**, 11169–11186.
149. Kresse, G. and Joubert, D. (1999) *Phys. Rev. B*, **58**, 1758–1775.
150. Rauh, H., Köhler, H., Geick, R., Nücker, N., and Lehner, N. (1981) *J. Phys. C*, **14**, 2705–2712.
151. Jenkins, J.O., Ure, R.W., and Rayne, J.A. (1972) *Phys. Rev. B*, **5**, 3171.
152. Bessas, D., Sergueev, I., Wille, H., Persson, J., Ebling, D., and Hermann, R.P. (2012) *Phys. Rev. B*, **86**, 224301.